PHYSICAL REVIEW A **80**, 033414 (2009)

Effects of high-flux neutron beams on ^{3}He cells polarized *in situ* with spin-exchange optical pumping

E. Babcock,[1,2,*] S. Boag,[3] M. Becker,[2] W. C. Chen,[4,5] T. E. Chupp,[6] T. R. Gentile,[5] G. L. Jones,[7] A. K. Petukhov,[2] T. Soldner,[2] and T. G. Walker[8]

[1]*Juelich Centre for Neutron Science, Garching 85747, Germany*
[2]*Institut Laue Langevin, Grenoble 38042, France*
[3]*ISIS, Chilton, Didcot OX11 QX, United Kingdom*
[4]*Indiana University, Bloomington, Indiana 47405, USA*
[5]*NIST, Gaithersburg, Maryland 20899, USA*
[6]*FOCUS, University of Michigan, Ann Arbor, Michigan 48109, USA*
[7]*Hamilton College, Clinton, New York 13323, USA*
[8]*University of Wisconsin, Madison, Wisconsin 55106, USA*

(Received 9 June 2009; published 17 September 2009)

Polarized ^{3}He produced by spin-exchange optical pumping (SEOP) has potential as a neutron spin filter for polarization and polarization analysis in many neutron-scattering and neutron particle physics applications. The advantage of the SEOP method is its suitability for providing continuous stable polarization over the course of long experiments. However, we have discovered that exposure to high neutron flux leads to additional strong relaxation mechanisms in the optically polarized alkali-metal vapor used to polarize the ^{3}He. At a neutron flux density of 4.7×10^9 cm^{-2} s^{-1}, the alkali-metal relaxation rate increased from 100 to 1000 s^{-1} leading to reduced alkali-metal polarization. Other effects such as time dependence and gas composition dependence were explored to help understand the processes. In this paper we discuss our observations and present possible solutions for practical use of SEOP as a neutron spin filter for high-flux density applications.

DOI: 10.1103/PhysRevA.80.033414 PACS number(s): 32.80.Xx, 33.25.+k, 03.75.Be, 29.25.Pj

I. INTRODUCTION

Polarized ^{3}He has applications as a neutron spin filter (NSF) in many areas of neutron science [1–3]. These include areas such as analyzers for small angle neutron scattering, reflectometry, wide angle detectors, diffraction, incident beam polarizers, and fundamental physics [4–10]. Fundamental physics experiments are a special subset of NSF applications that often require long measurement time and operation under higher flux conditions. This paper is a full report of experiments performed at the Institut Laue Langevin (ILL) that were initially reported in [11] looking at the effects on the spin-exchange optical pumping (SEOP) [12,13] method to polarize ^{3}He for the particularly demanding application of continuous polarization of ^{3}He in high-flux neutron beams.

Two methods are widely used to produce spin-polarized ^{3}He, SEOP and metastability exchange optical pumping (MEOP) [14,15]. Currently, MEOP can produce polarized ^{3}He with high polarization of up to $\simeq$75% for use as NSFs at rates of up to 1 bar·L h^{-1} to 2 bar·L h^{-1} [16,17]. This is done via optical pumping of low pressure gas ($\simeq$1 mbar) followed by mechanical compression to obtain the pressures used in NSFs [18]. Further fundamental work on increasing MEOP production rates by going to higher pressures and high magnetic field are being pursued [19,20].

The SEOP technique has also had recent developments including frequency narrowed diode array bars [21,22] and hybrid SEOP [23]. These techniques have increased production rates to several bar liters of polarized ^{3}He per day and have allowed an increase in the achievable polarization to 75% or greater for NSF similar to the MEOP technique [24,25]. In a recent demonstration that employed these developments, a polarization of 75% with a production rate of 2.4 bar·L per day was achieved with a fairly simple apparatus [26]. Because of the technical simplicity, these systems could be scaled up to produce more polarized ^{3}He per day for a polarized ^{3}He cell filling station or replicated to polarize more ^{3}He cells in a given time.

SEOP can be performed directly in permanently sealed cells in the typical pressure range of 0.6–4 bar used for NSFs, whereas gas polarized by MEOP at a typical pressure of around 1 mbar must be mechanically compressed [16,18]. The operation and design of SEOP systems to continuously polarize ^{3}He in sealed cells for neutron applications have been reported [27–30]. Not only does this eliminate the need for time-dependent corrections caused by the normal ^{3}He polarization relaxation rates but also eliminates the need to change the cells or cycle polarized gas on a routine basis. These features can be substantial advantages for long-term or precision measurements. Further, continuous polarization of the ^{3}He can provide higher time averaged polarization and provide protection from stray magnetic fields often present on polarized neutron instruments that can cause additional ^{3}He relaxation.

The majority of NSF applications to date have used either MEOP or SEOP to polarize the ^{3}He offline and thus in typical laboratory conditions. While efforts have been made to polarize the ^{3}He online using SEOP, most of this work has been done on neutron beams of relatively moderate to low flux or has been for analysis of weak scattered beams

---

[*] e.babcock@fz-juelich.de

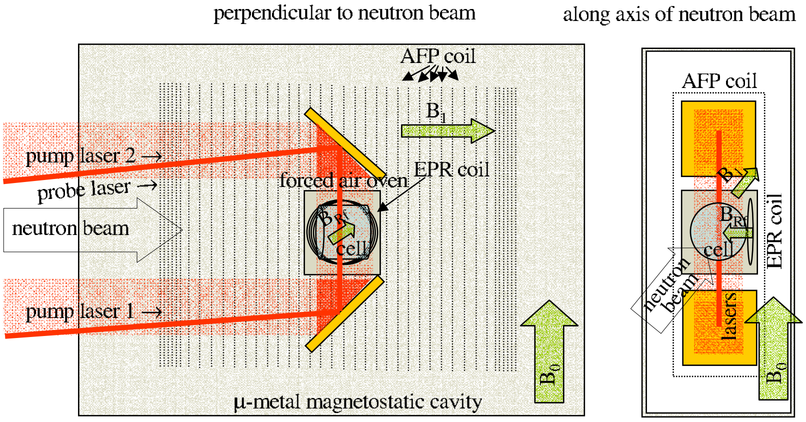

FIG. 1. (Color online) Diagram of the *in situ* SEOP apparatus. In contrast to other *in situ* polarizers with μ-metal shielding, this configuration allows the laser access to be perpendicular to the neutrons minimizing the equipment such as laser mirrors in the neutron beam. This is of special interest when working with beams of these flux levels. B_0 is the dc holding field (perpendicular to the neutron beam), B_1 is the strong sweepable rf field for adiabatic fast passage (AFP) of the ^{3}He spin (along the neutron beam), and B_{rf} is a weak orthogonal rf field for alkali-metal electron paramagnetic resonance (EPR) diagnostics.

[27–29]. The longest test of continuous SEOP on a beamline was obtained in operation of the polarizer for the NPDGamma experiment at the Los Alamos Neutron Science Center (LANSCE) which was operated for over a year at moderate flux [4,30]. The experience gained in that work, as well as interest to use a continuously polarized ^{3}He spin filter on the PF1B fundamental physics beamline [31] at the ILL, led to a collaborative effort to study SEOP in high-flux neutron beams.

Fundamental neutron physics experiments, i.e., experiments looking at fundamental neutron interactions or decays, such as NPDGamma or those on PF1B are typically neutron flux limited because of the small effects or asymmetries being measured. Hence, such experiments use slow neutrons (5 Å mean wavelength) to increase observation time and prefer operation on the highest flux neutron beams available. Therefore, these conditions require operation in a virtually unexplored regime for SEOP. In particular the effects of ionization from neutron absorption in the NSF cell have not been studied. In the NPDGamma experiment a reduction in ^{3}He polarization on the order of 2%–6% (relative) was observed when the *in situ* SEOP NSF system was exposed to a neutron capture flux density of $(1-3)\times 10^8$ cm^{-2} s^{-1} (see Sec. II B for a discussion of capture flux density). The observation of a decrease in ^{3}He polarization on the time scale of the spin-exchange time constant was later linked to a reduction in alkali-metal polarization [11,30]. In addition, a decrease in the maximum achievable ^{3}He polarization after months of exposure to the LANSCE beam was linked to increased opacity of the NSF cell walls to the laser light. The alkali-metal polarization in SEOP cells depends in a complicated way on alkali-metal relaxation rates and the spatially dependent optical pumping rates provided by the laser sources in a particular system [13]. Therefore, in order to further quantify this effect we recently measured the alkali-metal relaxation rates as a function of neutron flux.

This paper is a detailed report of experiments performed on the PF1B beamline to study the effects of high neutron flux on alkali-metal polarization in SEOP cells and is a follow up to Ref. [11]. Following an overview of the apparatus in Sec. II, we present our experimental observations in Sec. III. The following key results are presented. The alkali-metal spin-relaxation rates are greatly increased by the presence of the high-flux neutron beam. Upon initial exposure of neutron flux to the SEOP cell, there is a rapid initial increase in the alkali-metal spin-relaxation rate followed by a more gradual increase over a time period of several hundred seconds. At full ILL flux, the spin-relaxation rate can be an order of magnitude larger than the base relaxation rate in the absence of the neutron beam. Section IV is a first attempt to interpret these results and propose possible explanations.

II. APPARATUS

A. SEOP system and diagnostics

For this experiment we utilized an *in situ* SEOP polarizer [32,33]. It is comprised of a magnetic holding field, an oven to heat the cells to obtain the proper alkali-metal vapor pressure, two frequency narrowed optical pumping lasers, and many diagnostics. The diagnostics were similar to the ones developed and tested in prior fundamental SEOP laboratory studies [34]. However, they are not normally utilized in typical SEOP ^{3}He polarizer devices especially in *in situ* devices given the complexity, space, and radiation shielding requirements on neutron beamlines. Specifically, with these diagnostics we were able to measure ^{3}He polarization over time, pump-light absorption, alkali-metal polarization, and alkali-metal relaxation rates. A schematic of the apparatus is shown in Fig. 1.

The low-gradient ($\nabla B/B < 4\times 10^{-4}$ cm^{-1}) static magnetic holding field, called B_0, needed for preservation of the ^{3}He polarization was provided by a modified version of the μ-metal cavity described in [16]. This holding field basically consists of two parallel μ-metal pole plates connected magnetically by uniformly magnetized yokes also made of μ-metal on either side. Its main difference to that of the cavity in [16] is that B_0 is directed along the long direction of the rectangular cross section of the μ-metal cavity and that the yokes are magnetized by a uniform coil that is flush with the two pole plates instead of permanent magnets.

Two external-cavity frequency narrowed diode array bar lasers with a typical bandwidth of 60–80 GHz optically pumped the SEOP cells with over 50 W of light each. The principle of frequency narrowing is the same as in [22] except the output is taken off of a polarizing beam splitter cube (PBS) [28]. The PBS is placed directly after the half-wave plate that is located directly after the laser diode and used to adjust the fraction of feedback. In this configuration (Fig. 2) only about 30% of the light is incident on the diffraction

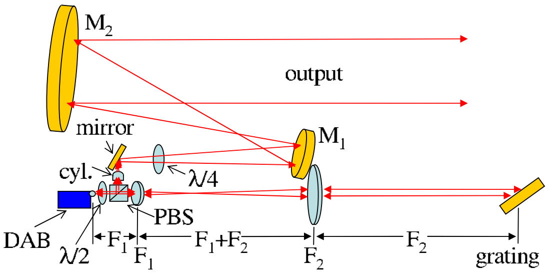

FIG. 2. (Color online) Schematic of lasers used for this experiment. This is a modification of the laser design in [35]. Focal lengths are $F_1=50$ mm, $F_2=200$ mm, cyl=10 mm (for the fast axis), $M_1=75$ mm, and $M_2=200$ mm or 300 mm. The grating is a 50 mm×50 mm high-modulation gold coated holographic grating with efficiency >90% at 795 nm.

grating, thus decreasing heating of the grating that leads to line broadening at high power intensities. The remaining 70% from the PBS is taken as the output and can be shaped easily and independently of the cavity optics. In this particular configuration the output is the reflected beam of the PBS which is typically only 95% polarized. While the absolute polarization of the optical pumping light is not critical for SEOP because light of the wrong polarization is rapidly attenuated by the cell, utilizing the transmitted beam or another type of beam splitter such as a Wollaston prism which can provide polarization of over 99.99% could increase the efficacy of the laser. We have successfully implemented such modifications in subsequent versions of the laser cavity. The only other modification in this laser cavity from that of [22] is the use of a high efficiency (>90%) gold coated high modulation grating which had a linear groove density of 2150 mm^{-1}.

The gratings had a motorized screw in the diffraction grating mounts that allowed us to tune the diffraction angle and thus wavelength of the spectral peak of the lasers remotely. A real-time spectrometer with a 0.07 nm spectral resolution was installed to optimize the laser narrowing and tune the wavelength to the Rb resonance. This same spectrometer could be used to observe the spectral transmission of the pump light through the SEOP cell provided only one optical pumping laser was in operation.

The collimating and expansion of the beam to the size of the cell is done with only three focusing optics. A 10 mm cylindrical lens was placed shortly after the PBS, making the divergence of the fast axis of the laser, which is collimated by a factory installed microlens at the face of the laser, similar to that of the slow axis (divergence ≃15°). This allows final collimation and expansion to be done with spherical optics. After some distance for expansion, the beam is collimated and magnified with a telescope made of two large diameter spherical mirrors. Configurations utilizing lenses instead of mirrors can also be used and since the beam is a diverging rectangle after the cylindrical lens, final collimation can also be done with a single spherical optic making this laser configuration very robust. For this experiment two different telescopes were used with the focal lengths of $M_1=75$ mm and $M_2=200$ mm or 300 mm yielding magnifications of 3× or 4× for beam sizes of 6 cm×8 cm and 7 cm×10 cm, respectively. A diagram of the lasers and coupling scheme is given in Fig. 2.

The optical pumping cells were contained in a forced air-heated oven made of calcium silicate rigid insulation board to reach the 170 °C to 210 °C temperatures needed to maintain the appropriate alkali-metal vapor densities. The oven had double 0.7-mm-thick Si-crystal windows on the front and back for neutron access and double 1-mm-thick borofloat glass windows on the top and bottom for optical access along the direction of B_0. The heating was done by a 1.5 kW air process heater connected to the oven via glass and copper tubes and controlled with a nonmagnetic thermocouple probe and a proportional-integral-derivative temperature controller. This oven along with two mirrors placed at 45° to direct the laser light along the B_0 direction were mounted inside a frame that also held a rectangular solenoid coil for AFP inversion of the ^{3}He polarization [36]. The AFP coil was installed for other neutron applications of the polarized ^{3}He and was not used for these tests.

The probe laser used for alkali-metal diagnostics entered slightly off axis and utilized the same 45° mirrors as the pump beams to direct it into and out of the cell. The probe laser was detuned about 1 nm from the Rb D$_2$ ($5s_{1/2} \to 5p_{3/2}$) resonance. During measurements involving the probe laser only one pump laser was used and the beams propagated in the opposite directions to help separate them. The polarization of the probe is sensitive to the electron spin polarization of the alkali atoms through the Faraday effect, thus it provides a rotation angle which is proportional to the alkali-metal polarization and number density. Over small angles, the signal from the subtracting photodiode detectors in the polarization analyzer is linear with the alkali-metal polarization. The probe beam, after exiting the magnetic cavity, was picked up with a mirror which directed the light into a light polarization analyzer constructed from a half-wave retarder, a polarizing beam splitter cube, and a pair of subtracting photodiodes. An electron paramagnetic resonance (EPR) coil was tuned to the radio frequency EPR transitions of the K atoms and allowed us to measure the alkali-metal polarization (P_A) with the method given in [34]. By sweeping the rf about the EPR transition frequencies for our B_0 field and observing the rotation of the probe laser polarization as the rf became resonant with the Zeeman transitions of the K atoms one can determine the relative populations of the individual m_f magnetic sublevels from the peak areas. Assuming a spin-temperature distribution one can then determine the absolute P_A from the ratios of relative peak areas [37].

The measured alkali-metal spin-relaxation rate (γ_A) was determined with the relaxation in the dark method [38]. Again a single pump beam is used; here it is kept at low intensity so that the alkali-metal polarization is intentionally low. The starting value of the alkali-metal polarization is known to be low by comparison of the amplitude of this signal to that when the laser is at high intensity. The pump light is then chopped with a mechanical shutter at a rate of <1 Hz providing periodic exponentially decaying transients in the alkali-metal polarization. This signal was collected and averaged using a data acquisition card on a personal computer and the spin-relaxation rate was inferred from the time constant of the decay.

TABLE I. List of cells and their parameters used in this experiment. All cells are blown from GE180 [40] glass and are cylindrical except for cell Fanny, which is a spherical cell with a diameter of 6 cm. The value of $d\gamma_A/d\sqrt{\phi_n}$ is the rate of change in the measured, or total, alkali-metal relaxation rate vs the square root of the incident flux density ϕ_n (relative standard uncertainty $\simeq 5\%$). Here $s\gamma_A$ is the true spin-relaxation rate accounting for coupling of the electronic spin to the nuclear spin where s is the slowing-down factor which can be calculated [41]. $\int A_n d\lambda$ is the wavelength integrated neutron absorption of each cell calculated for the PF1B neutron energy spectrum. The ^{3}He and N_2 partial pressures are given in bar at 25 °C.

Cell name	^{3}He (bar)	N_2 (bar)	$L\times W$ (cm^2)	$\int A_n d\lambda$ (%)	$d\gamma_A/d\sqrt{\phi_n}$ (10^{-3} cm s$^{-1/2}$)
Cell Orvieto (K-Rb)	1.10	0.07	7×9	91	1.55
Cell Lottie (Rb)	0.8	0.1	8×7	87	1.63
Cell Lucky Luke (Rb)	0.52	0.12	6×6	67	1.62
Cell Lykurgos (Rb)	2.54	0.12	6×6	98	1.52
Cell Fanny (Rb)	1.0	0.5	$6=D$	86	2.87

Relative ^{3}He polarization (P_{He}) over time was monitored with a simple, home-made, single coil pulse and acquire nuclear magnetic resonance (NMR) free induction decay (FID) system. This system consists of a 300 turn, 2 cm diameter coil tuned to resonate at the ^{3}He Larmor precession frequency, 32 kHz in our case, which was placed on the side of the SEOP cell orthogonal to both the neutron beam and the B_1 field. A high speed 125 kHz computer based data acquisition card with analog input and output is used to send a low amplitude tip pulse to cause a small precession of the ^{3}He atoms next to the coil, then after the ring-down of the coil, the FID signal is recorded and filtered with software to subtract noise and obtain the FID signal strength which is proportional to P_{He} polarization.

This relative value of P_{He} was then calibrated absolutely with neutron time-of-flight (TOF) measurements [30,39]. TOF on a continuous neutron source is performed by placing a mechanical neutron chopper in the beam and measuring the neutron count rate vs time on a detector some distance after the chopper. To provide the needed wavelength resolution the open duty cycle of this chopper is about 1%. Since the neutron wavelength is related to its velocity by the de Broglie wavelength, by triggering the detector on the opening edge of the chopper and knowing the chopper to detector distance one can then convert the counts vs time to counts vs neutron wavelength or energy. With the addition of relative P_{He} information obtained from NMR FID, one can determine the absolute P_{He} by performing TOF transmission at any two arbitrary values of relative ^{3}He polarization. Each TOF transmission measurement has a $T_0(\lambda)\cosh(P_{\mathrm{He}}\Theta\lambda)$ dependence where $T_0(\lambda)$ is the empty cell transmission for the arbitrary neutron spectrum, Θ is the product of ^{3}He density, neutron absorption cross section and target (cell) length, and λ is the neutron wavelength. Thus taking the ratio at two relative values of P_{He}, known from uncalibrated FID, one obtains a one parameter fit for P_{He} vs λ without having to depolarize the gas in the cell as is normally done for absolute ^{3}He polarimetry.

Several cells were used for this experiment. Their parameters are given in Table I and represent a partial range of gas pressures and compositions typically used in SEOP NSFs. Two of the cells were studied extensively, cell Lottie a pure Rb cell [42] constructed at ISIS, and cell Orvieto a K-Rb hybrid cell [25] constructed at NIST. The cells are identified in this work, and in prior references, by the names listed in Table I.

B. Beamline and flux measurement

We chose to use the fundamental physics beamline PF1B at the ILL because it is a candidate for an *in situ* polarizer as an instrument option. PF1B's high neutron flux intensity and large beam size as well as its open experimental area made it ideal for this experiment [31]. A diagram for the installation is given in Fig. 3. At the exit of the PF1B super mirror (SM) neutron guide the beam intensity could be reduced with B_4C plastic "Swiss cheese" beam attenuators. These attenuators are simply sheets of B_4C rich plastic, which is 100% absorbing for the neutrons at our wavelengths, with a series of small holes distributed evenly over the area of the beam to allow neutron transmission of approximately 1%, 10%, or 100% (no attenuator). After this, an additional 4 m SM extension guide with a (7×11) cm^2 cross section was installed. The 1° divergence of the neutron beam combined with the length of the guide after the Swiss cheese attenuators ensured a spatially uniform beam at the NSF cell. The extension guide stopped approximately 100 cm before the SEOP cell. Final beam size and collimation were determined by B_4C rich rubber masks placed at the exit of the neutron

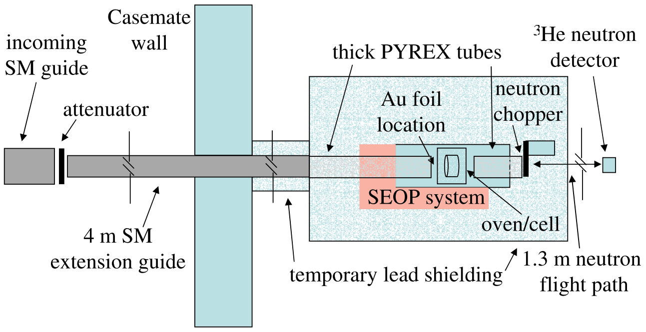

FIG. 3. (Color online) Diagram of the experimental setup on PF1B.

guide and directly before the SEOP oven. About 60 cm after the SEOP oven, a small disk neutron chopper was installed for TOF measurement of the neutron spectrum. To limit the amount of neutron scattering from the air, thick boron-containing glass (Pyrex) tubes with thin aluminum foil windows for neutrons were filled with ^{4}He. These ^{4}He filled tubes were placed between the SM extension guide and the SEOP oven and between the SEOP oven and the neutron chopper.

A "thin" neutron detector [i.e., a detector with a low relative neutron absorption$=1-\exp(-n\sigma l)$ where n is the absorbing atom number density, $\sigma(v)$ is the neutron absorption cross section as a function of neutron velocity v, and l is the length along the beam] is then installed 130 cm after the chopper. To adapt to the different attenuators and avoid saturation of the detector count rate, detectors with the efficiencies $\simeq 2.4\times 10^{-6}$ and $\simeq 1\times 10^{-4}$ were used. The two detectors were calibrated against each other at the 1% flux level. These relative values of capture flux were then scaled to absolute values of capture flux by a gold foil calibration at the front of the SEOP oven.

Gold foil activation is a well known method to measure capture flux density of a neutron beam. Au has a single isotope, ^{197}Au, with a well known neutron absorption cross section of 98.7 b at 1.8 Å, for which the neutron absorption reaction produces ^{198}Au. The ^{198}Au decays to ^{198}Hg which has a half life of 2.69 days emitting a beta particle and a 0.411 MeV gamma photon [43]. The neutron capture flux density is thus determined by exposing a Au foil of calibrated mass for a known amount of time, 10 min in our case, and then measuring the beta or gamma emission rate of the activated foil after a known waiting time (several days in our case). The accuracy of this measurement is typically 10%. The reactor power was steady over the course of the measurements and further corrections were not necessary.

Consequently the neutron capture by thin detectors such as our low efficiency neutron detectors or Au foil is weighted by the $1/v \propto \lambda$ absorption cross section of the ^{3}He, ^{6}Li, or Au atoms, respectively, in our neutron detectors or Au foil [31]. The neutron cross sections are normally expressed for the reference wavelength of $\lambda=1.8$ Å which has a neutron velocity of $v=2200$ m s^{-1}. This corresponds to the maximum in intensity of a thermal neutron spectrum (i.e., a spectrum with a Boltzmann distribution of temperature 25 °C) and thus must be scaled by a given beam's wavelength spectrum, which is not necessarily a Boltzmann distribution, to compare it to the actual neutron particle flux density. In general the measurement of capture flux is relevant for fundamental physics experiments, such as neutron decay experiments, because the probability of neutron decay is proportional to the time spent in the apparatus and thus the wavelength. However, in our experiment most of the neutron beam is absorbed (see Table I), consequently, the actual neutron particle flux density, which we will simply call flux density, is more relevant to this study.

To convert a given capture flux density from a thin detector to flux density, one must know the neutron spectrum vs wavelength. The neutron spectrum was thus measured by TOF as described above in Sec. II A using the low efficiency neutron detector giving the distribution of relative capture flux vs wavelength which we then normalized to the capture flux density of 1.4×10^{10} s^{-1} cm^{-2} measured with the Au foil. The spectrum was then corrected for the $1/v$ dependence of the cross section by scaling the intensity vs λ by $1.8/\lambda$ where λ is in angstrom and 1.8 Å is the reference wavelength of the Au absorption cross section. Finally the resulting spectrum was integrated to obtain a flux density of 4.7×10^{9} cm^{-2} s^{-1}. The neutron absorption listed for the cells (see Table I) thus refers to the absorbed fraction of this flux density.

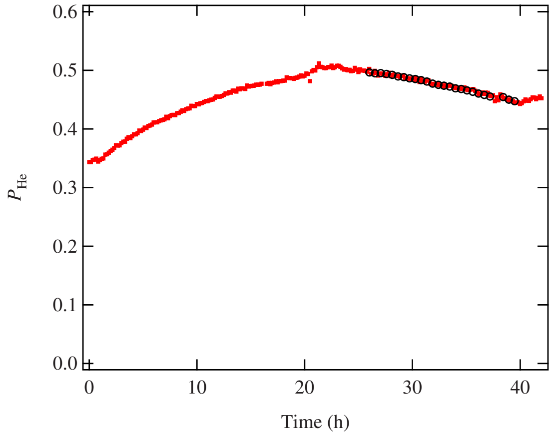

FIG. 4. (Color online) The relative P_{He} via NMR FID (solid red squares) for the cell Orvieto. The data show a spin-exchange time constant of 13.6 h. At a time near 20 h, the cell was exposed to a neutron flux density of 4.7×10^{9} cm^{-2} s^{-1}. The polarization drop was then monitored with neutron TOF transmission (black open circles) while continuing the NMR FID measurements. At a time near 40 h the neutron beam was closed and P_{He} began to recover with the spin-exchange time constant.

Some additional measurements were also done on a thermal high-flux test beamline at the ILL (ILL tomography station). While this beam had a thermal spectrum with mean wavelength of 1.8 Å compared to the 5 Å mean wavelength on PF1B, it had a similar flux density of 2.4×10^{9} cm^{-2} s^{-1}. This value was measured with a gold foil as described above and by assuming a typical thermal intensity distribution of the spectrum as was indicated in prior work on this beamline [44]. This beamline is simply a large area high-flux thermal beam obtained by a direct view of the thermal moderator tank and thus contains a significant fraction of fast unmoderated neutrons and gamma rays from the reactor. We collimated this beam to the size of our SEOP cells with stacks of boron containing rubber in a 50-cm-long collimator.

III. MEASUREMENTS AND RESULTS

A. ^{3}He polarization drop

The first measurements involved polarizing the hybrid cell Orvieto and observing the changes under exposure to neutron flux. As shown in Fig. 4, which was obtained with our calibrated NMR FID system described in Sec. II A, the ^{3}He in the cell was polarized to a relatively high level of $P_{\mathrm{He}}=50\%$ with an extrapolated maximum of 55%. This polarization was limited by the wall relaxation of this cell, which depends on the orientation of the cell with respect to the magnetic field and is larger than in cells one would normally use to obtain a high degree of ^{3}He polarization [45]. For the orientation of the cell during the experiment the room temperature ^{3}He relaxation time was only 50 h whereas a maximum of 90 h had been observed in the laboratory in a different orientation. Because of our main interest in alkali-metal polarization for this experiment, the limit to the ^{3}He performance from wall relaxation for this cell was not critical.

The cell was then exposed to the full intensity of the beam on PF1B. P_{He} was again monitored using NMR FID and now also with neutron TOF transmission measurements. The given equilibrium or steady-state value of P_{He} is proportional to P_{A} and the rate balance between the ^{3}He spin-exchange rate γ_{SE} and the total ^{3}He relaxation rate Γ_{He} for the same conditions,

$$P_{\mathrm{He}} = P_{\mathrm{A}} \frac{\gamma_{\mathrm{SE}}}{\Gamma_{\mathrm{He}}}. \tag{1}$$

Here $\gamma_{\mathrm{SE}} = \kappa_{\mathrm{Rb}}[\mathrm{Rb}] + \kappa_{\mathrm{K}}[\mathrm{K}]$ for a hybrid cell or just $\gamma_{\mathrm{SE}} = \kappa_{\mathrm{Rb}}[\mathrm{Rb}]$ for a Rb only cell where κ_{Rb} and κ_{K} are the respective Rb and K ^{3}He spin-exchange rate coefficients and [Rb] and [K] are the densities of each species [23]. $\Gamma_{\mathrm{He}} = (1+X)\gamma_{\mathrm{SE}} + \Gamma_{\mathrm{cell}}$ where X is an extra ^{3}He relaxation mechanism which appears to be proportional to the alkali-metal density [46] and Γ_{cell} is the sum of the ^{3}He dipole-dipole self-relaxation, cell wall-induced ^{3}He relaxation, and ^{3}He relaxation from magnetic-field gradients [47]. Γ_{He} is thus the observed rate of change of P_{He} for buildup or decay. At room temperature, $\Gamma_{\mathrm{He}} = \Gamma_{\mathrm{cell}} = 1/T_1$ because the alkali-metal density and thus spin-exchange rate are essentially zero, hence T_1 is the often cited time constant of the decay of P_{He}. From Eq. (1) we can see how the equilibrium value of P_{He} changes with P_{A} and that if Γ_{cell} is fixed, i.e., there are no additional terms from direct ^{3}He relaxation, that the rate of change of P_{He} from one steady-state value to another must occur at Γ_{He}. Other experiments at the ILL using MEOP polarized ^{3}He seem to suggest that direct ^{3}He nuclear spin relaxation would not be observable in SEOP NSFs on the time scales of $\Gamma_{\mathrm{He}}^{-1}$ due to the presence of N_2 buffer gas [48]. This is in agreement with expectations from earlier work with charged particle beams. They showed that ionization produced in the polarized ^{3}He target by the particle beams allowed the formation of $^3\mathrm{He}_2^+$ molecules which caused rapid nuclear depolarization of the ^{3}He. This process could be effectively quenched by modest amounts of buffer gas such as N_2, always present in sufficient quantities in a SEOP polarized cell, which acts as a third body to break up the $^3\mathrm{He}_2$+ molecules [49].

We experienced difficulties with the time stability of our optical pumping lasers due to environmental heating particular to this installation. This caused the efficacy of the lasers to decrease during this measurement. This also accounts for the apparent changes in polarization rate at approximately 2 and 19 h (see Fig. 4). Thus, no accurate data can be obtained about the rate of change in P_{He} from this measurement alone other than to conclude the alkali-metal density could not have been substantially different for the neutron beam on or off. However, the prior measurements at LANSCE measured γ_{SE} several times with the beam on and off. They found γ_{SE} to be the same with the neutron beam off and on, implying that [Rb] was the same in both instances and that the magnitude of the change in P_{He} was proportional to the change in P_{A} [11]. We cannot determine conclusively that the alkali-metal density is not being modified by chemical reactions due to ionization and charged particles in the cells in the times scales longer than this experiment. However, the cell Lykurgos, in prior testing, was exposed to the PF1B beam for over 1 week in the absence of optical pumping and cells used in the NPDGamma experiment retained expected alkali-metal vapor pressure for a given temperature when measured in the laboratory after the prolonged neutron exposure. Thus, we postulate the change in P_{A} is the dominant effect. Measurements presented in Secs. III B–III D on the changes in P_{A} and its cause are thus the main experimental focus of this work.

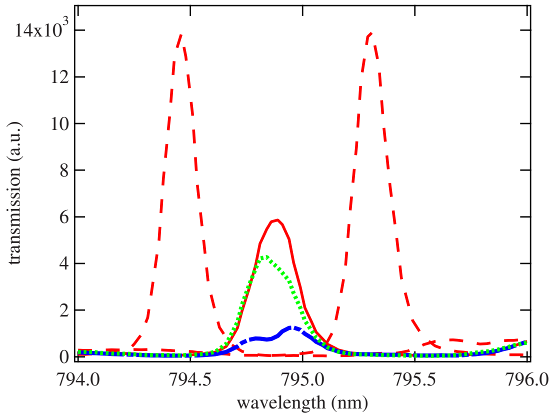

FIG. 5. (Color online) The relative pump light transmission with one laser. The dashed red lines show data for the laser tuned off resonance (i.e., zero absorption) to determine the relative transmission. The spectrometer resolution was 0.07 nm. For 0%, 8.5%, and 100% of the PF1B flux, the respective transmissions were 54% (solid red line), 42% (dotted green line), and 14% (dot-dash blue line).

B. Pump light absorption

As described in Sec. II A, the relative cell transmission (T) for the optical pumping light of one pump laser was observed spectrally with a real-time spectrometer. As shown in Fig. 5, the transmission decreased dramatically as the neutron beam flux was increased. In order to understand this one must consider the properties of light propagation in an optically pumped media.

Not including relaxation, the on-resonant light absorption (A) of a dense polarized alkali-metal vapor with polarization $P_{\mathrm{A}}(\vec{r})$ is given by

$$A = 1 - T = \mathcal{R}(\vec{r})[1 - P_{\mathrm{A}}(\vec{r})]. \tag{2}$$

Here $\vec{r}$ represents the location in the cell along the path of the optical pumping light, $\mathcal{R}(\vec{r}) = \int d\nu \Phi(\vec{r},\nu)\sigma_{\mathrm{A}}(\nu)$ is the pumping rate that depends on $\Phi(\vec{r},\nu)$, the laser intensity per unit frequency, and the alkali-metal absorption cross section $\sigma_A(\nu)$. Writing $\Phi(\nu)$, $\mathcal{R}$ and P_A as a functions of $\vec{r}$ here is simply to remind us that these quantities are all functions of cell position. To obtain explicit estimates of A or $\mathcal{R}$ along the path of the light propagation, numerical modeling for a given set of conditions that includes relaxation must be performed. However, here we present the conceptual argument to interpret the data.

For typical SEOP conditions the optical thickness $[\mathrm{Rb}]\sigma_A l > 100$, where [Rb] is the Rb density and l is the cell length and the relative absorption is simply $1-\exp(-[\mathrm{Rb}]\sigma_A l)$ for an unpolarized alkali-metal. Thus the light is attenuated within a small fraction of the cell for an unpolarized vapor. For a polarized vapor, the absorption given by Eq. (2) is much less since for nearly fully polarized atoms $1-P_A \ll 1$. Consequently, the light intensity is only gradually reduced as the beam propagates through the cell provided $P_A(\vec{r})$ is high everywhere in the cell. If $P_A(\vec{r})$ begins to be compromised at some position in the cell, the on-resonance absorption for the whole cell quickly becomes large. For broadband laser sources, the frequency spectrum of the light also varies with position in the cell, because on-resonant frequency components are depleted more rapidly than those that are off-resonance. But for an optical pumping source of width comparable to the atomic absorption width, the spectral modifications of the laser are less dramatic.

The pressure broadened line width is about 20 GHz for most cells in this experiment [50] compared to our pump laser linewidth of 60–80 GHz. This fact, combined with the resolution of the spectrometer, means that a so-called spectral hole where all the on-resonant light is depleted is not apparent in the data of Fig. 5, except perhaps at the highest neutron flux. Nevertheless, the large increase in absorption at high flux is a clear indication that P_A has been compromised causing the cell to attenuate nearly all the useable light due to the effects of the neutron absorption.

C. Alkali-metal polarization drop

The drop in alkali polarization was explicitly observed by measurement of the EPR spectrum of the alkali atoms. Alkali-metal polarization is given by

$$P_A(\vec{r}) = \frac{\mathcal{R}(\vec{r})}{\mathcal{R}(\vec{r}) + \Gamma_A}, \qquad (3)$$

where Γ_A is the full alkali-metal spin-relaxation rate. Thus, we can see the straightforward relation between alkali-metal polarization and relaxation. However, we point out obtaining strict quantitative information relating the two is difficult because $\mathcal{R}(\vec{r})$ depends on the optical pumping laser spectrum and intensity as discussed above in Sec. III B whereas our alkali-metal polarization measurement is taking a line average of P_A over the whole path of the optical pumping light in the cell.

For this measurement both lasers and the cell Orvieto were used. The scope traces of the EPR spectra are shown in Fig. 6. The deduced alkali-metal polarization vs flux is shown in Fig. 7. As one can see, the alkali-metal polarization changed by as much as 15% for the highest flux. This measurement was done at $P_{\mathrm{He}}=0$ to eliminate ambiguity arising from the roughly 10%–20% change in captured neutron flux from polarized to unpolarized ^{3}He for the levels of polarization attainable in this experiment. These measurements could only be done in the hybrid cell since for our μ-metal cavity the B_0 field is limited to about 2 mT (20 G) because of saturation in the μ metal. At this field the EPR resonances for Rb are not resolved. We chose a B_1 field of 1 mT (10 G) for these tests which is more than sufficient to resolve the EPR resonances of the K in a hybrid SEOP cell. As can be seen in Fig. 6, since the ^{87}Rb lines are not resolved the relative area of this peak, on the far left, remains unchanged whereas the areas of the ^{39}K and ^{41}K $m_f=-1\rightarrow-2$ peaks become smaller and the area of the ^{39}K $m_f=0\rightarrow-1$ peak becomes larger. The ^{41}K $m_f=0\rightarrow-1$ peak is not visible but would be in the left shoulder of the ^{39}K $m_f=-1\rightarrow-2$ peak. Again, we conclude that the neutron beam is causing a substantial reduction in the alkali-metal polarization.

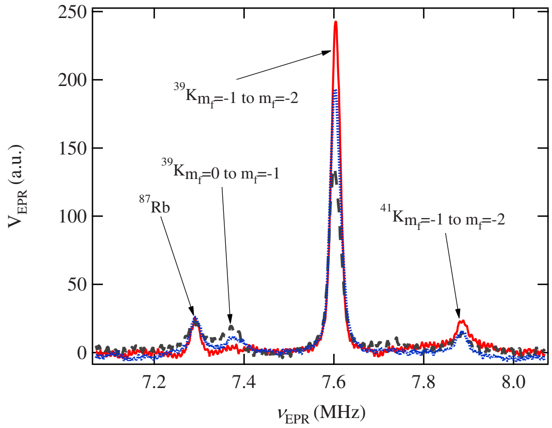

FIG. 6. (Color online) EPR spectra for no incident neutron flux (solid red line), 8.5% flux (dotted blue line), and full flux (dashed black line) for the cell Orvieto.

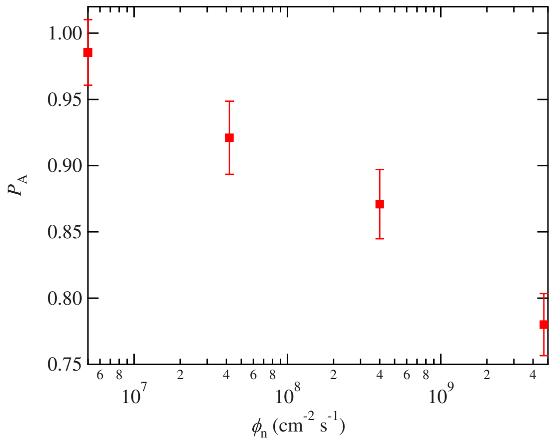

FIG. 7. (Color online) The measured alkali-metal polarization vs the neutron flux density on a log x scale, the zero-flux point has been offset to display it on this plot. The four points from left to right represent zero flux, 0.89% flux, 8.5% flux, and 100% flux. The error bars indicate the standard uncertainty in the determinations of alkali-metal polarization.

D. Alkali-metal relaxation for different cells

The reduction in alkali-metal polarization observed in the experiments above strongly suggests that the neutron beam increases the spin-relaxation rate of the alkali atoms. The increased spin-relaxation rate is then responsible for the increased absorption of the pump laser light and corresponding lowering of P_A. Consequently, the most direct measure of the neutron beam effects is to measure the alkali-metal spin-relaxation rates which was done as described earlier in Sec. II A using the relaxation in the dark method [38].

In general, the alkali-metal spin relaxation in a SEOP cell, Γ_A, is the sum of the relaxation rates from collisions with the various atomic or molecular species in the cell. For a pure Rb cell these rates include $\Gamma_{\text{Rb-Rb}}$, $\Gamma_{\text{Rb-N}_2}$, and $\Gamma_{\text{Rb-He}}$. For a hybrid cell there are the additional equivalent terms for the K atoms, plus a $\Gamma_{\text{Rb-K}}$ term. The measured spin-relaxation rate for the Rb atoms depends on all of these cross sections which are functions of the density of each species and the temperature. A complete discussion of these relaxation rates for pure Rb and hybrid K-Rb cells is given in Ref. [26]. The relaxation rates at zero neutron flux varied from cell to cell in this experiment because of their different parameters, thus the effective relaxation caused by the absorbed neutron flux was measured as a function of neutron flux. Assuming the other cross sections are unmodified by the presence of the neutron flux, these zero-flux relaxation rates are just an offset.

During the course of these measurements we observed that upon first turning on the neutron beam the spin-relaxation rate increased suddenly on a time scale much less than the typical 30 s data acquisition rate for the signal averaging needed for each trace. Subsequent measurements were made on the thermal high-flux test beamline described in Sec. II B. This beamline had a fast secondary neutron shutter with a <1 s opening/closing time which could be triggered by an external source. With the alkali-metal highly polarized, $P_A \simeq 1$, we simply observed the Faraday rotation signal of the probe laser as the fast neutron shutter was pulsed. Within measurement accuracy the alkali-metal polarization dropped quickly coincident with the shutter opening after which it began to decrease more with a slow time constant. While the magnitude of the polarization drop was not calibrated, it implies the fast increase in alkali-metal relaxation, accounting for a significant fraction of the measured increase, occurs on the time scale of 1 s or faster.

After the initial fast increase, the relaxation rate continued to increase slowly with a 200–350 s time constant before reaching a steady-state value at roughly double the initial rapid increase in relaxation rate. Similarly, when the beam is shuttered off after a lengthy illumination period, the relaxation rate quickly drops by a factor of about 2 and then slowly returns to the natural relaxation rate of the cell. For the 0.07 and 0.1 bar $[N_2]$ cells Orvieto and Lottie, the fraction of the fast increase was about equal to the additional slow increase in alkali-metal relaxation rate, whereas the 0.5 bar $[N_2]$ cell Fanny perhaps had about a 25% fast increase and 75% slow. The behavior is illustrated in Fig. 8. The precise value of the time constant for the slow buildup in the relaxation varied from cell to cell and there is not comprehensive data on all the cells. Due to the time and technical constraints of this particular measurement, more information on the properties of the fast and slow components was not obtained. Given the limited amount of data available, it is unclear how the time constant may vary given different cells of different parameters or if it changes as a function of neutron flux density.

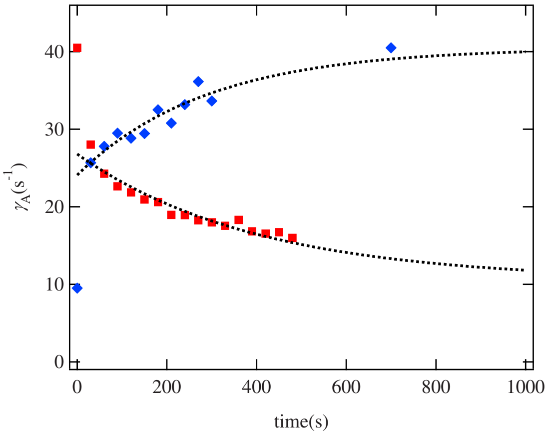

FIG. 8. (Color online) The measured alkali-metal relaxation rates averaged over 30 s vs time after the opening (blue diamonds) or closing (red squares) of the neutron beam. These particular data were for cell Orvieto at 8.5% flux or 4×10^8 cm^{-2} s^{-1}. The dotted black lines show exponential fits to the data with the offsets held to the steady-state value. The values of the time constants for these data sets are 290 s and 400 s, respectively, for the slow time buildup and decay of alkali-metal relaxation.

More experiments should be done to explore the relative fraction of the fast increase in alkali-metal relaxation vs the additional slow buildup and both should be measured separately as a function of incident neutron flux density and gas composition. Subsequent analysis of data taken in this experiment, discussed in Sec. IV B, has led us to hypothesize the N_2 may be involved in cluster formation, and consequently perhaps relevant to the slow time constant. Thus, N_2 dependence is of particular interest for future study.

A number of measurements of steady-state spin-relaxation rates after the beam had been on for a long time (>10 min) for different cells and different neutron flux densities are shown in Fig. 9. As can be seen the alkali-metal relaxation appears to closely follow a $\sqrt{\phi_n}$ dependence where ϕ_n is the incident neutron flux density. This $\sqrt{\phi_n}$ dependence will be discussed in Sec. IV. This information is also summarized in Table I. Nearly all of the cells tested showed the same dependence of the alkali-metal relaxation rate with flux density, even despite the different base (zero flux) relaxation rates caused by the varying gas compositions and alkali-metal vapor compositions.

As a check on the consistency of these relaxation measurements with the polarization and absorption results, we note that the relaxation measurements imply a photon absorption rate estimated as

$$[\text{Rb}]s'_A \gamma_A P_A V = 5 \times 10^{19} \text{ s}^{-1} \quad (4)$$

from neutron-induced relaxation, i.e., one photon is absorbed for each alkali-metal atom relaxed for ideal alkali-metal op-

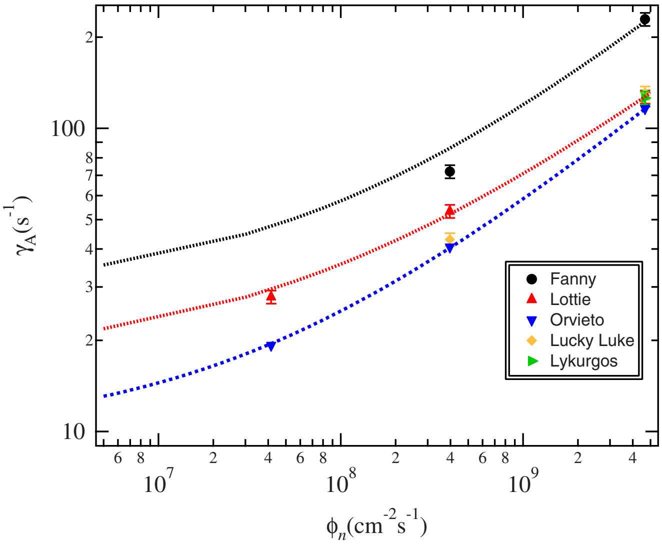

FIG. 9. (Color online) The measured alkali-metal relaxation rates vs flux density on a log-log scale. The zero-flux values of γ_A were 29 s^{-1} for cell Fanny, 17.2 s^{-1} for cell Lottie, 9.7 s^{-1} for cell Orvieto, 17.5 s^{-1} for cell Lucky Luke, and 21.8 s^{-1} for cell Lykurgos. The data for the cells Orvieto (K-Rb) and Lottie (Rb) are fit to a power fit. The fits shown have power relations of 0.508 ± 0.006 (lower line) and 0.47 ± 0.02 (middle line) for cell Orvieto and cell Lottie, respectively. The data for the cell Fanny have a line with a power of 0.5 added to guide the eye (upper line). The zero-flux values of each of these lines were held to the measured values of the respective cell. The error bars are errors of the fits of the individual exponential decays. The scatter in the middle data points may be due in part to the repeatability of the installation of the neutron attenuator used for this (8.5%) flux.

tical pumping. Here $\gamma_A = \Gamma_A / s'_A$ is the measured alkali-metal spin-relaxation rate where Γ_A is again the full alkali-metal spin-relaxation rate, [Rb] the Rb density, and V the cell volume. The factor s'_A is the slowing-down factor in the high polarization limit, which is 5.44 for a pure Rb cell, where the slowing-down factor is from the coupling of the electron spin to the nuclear spin and represents the effect of the angular momentum stored in the alkali-metal nucleus. The slowing-down factor is a function of the alkali-metal polarization and nuclear spin and can be calculated as a function of P_A for a given isotopic composition as in [41]. Since we measure the electron spin-relaxation rate we must include this angular momentum stored in the nucleus to arrive at the photon consumption rates. This photon absorption rate is a remarkable number when we consider that the maximum neutron absorption rate over the whole cell is only 1.5×10^{12} s^{-1}. Each absorbed neutron is apparently catalyzing through some process the removal of more than $3 \times 10^7 \hbar$ of angular momentum from the alkali atoms where $\hbar = h/2\pi$ and h is Planck's constant. Given one resonant photon will be absorbed for each alkali-metal atom relaxed the numerical factor in Eq. (4) corresponds to about 8 W of laser power at 795 nm, thus it is consistent with the before mentioned observations in Sec. III B.

For the case of the pure Rb cells with 0.1 bar to 0.12 bar N_2 partial pressure at 170 °C we obtained similar measured relaxation rates as a function of neutron flux density despite a factor of 5 variation in ^{3}He density (see Table I). However, we point out that the cells were relatively "thick" for our neutron energy spectrum, i.e., the number of captured neutrons was only varying by about 31% from the lowest to highest ^{3}He pressure. The only cell with a significantly different neutron-induced alkali-metal relaxation rate was the high N_2 pressure cell Fanny. Cell Fanny had 0.5 bar N_2 and had nearly twice the extra alkali-metal relaxation at full flux. The origins of this effect will be explored more in a future experiment.

E. Cell whitening

Previously it has been noted that a white film forms in the cell after several months of exposure to a cold neutron beam, i.e., 5 Å mean wavelength, with a capture flux density of $(1-3) \times 10^8$ cm^{-2} s^{-1} [30]. Note, this value of capture flux density must be divided by approximately a factor of 3 (5/1.8, the ratio of the mean wavelengths of the two beams) to compare it to the values we cite for neutron flux density on PF1B (see Sec. II B). In that work, the beam diameter was 9 cm, hence the total number of neutrons absorbed in the cell was of the order of 10^{17} per year and it was exposed to neutron flux for approximately 0.75 year of a 1.5 year data run. This film caused reduced ^{3}He polarization due to decreased transmission for the optical pumping light. During the course of this experiment, we had two cells exposed for significant times, cell Lottie and cell Orvieto. The hybrid cell Orvieto was exposed for ≈20 h at full flux and hence a total neutron absorption of $\leq 10^{16}$ for a 8 cm neutron beam diameter while held at an operating temperature of 210 °C. The pure Rb cell Lottie was not exposed for as long, less than 2 h total, and held at an operating temperature of 170 °C.

Despite the shorter exposure time the pure Rb cell began to show signs of a white film forming, whereas the K-Rb cell only had a small amount of white film in an area of the cell where a blockage of hot air flow by the cell mount may have caused a cold spot on the cell. Although the exact details of the difference in the chemistry of the two cases have not been explored, it could be a formation of RbH particles, or perhaps alkali-azides (i.e., RbN_3). H (and T) ions are formed by the neutron absorption, although at very small concentrations, and a significant amount of ionized N_2 would be created but one would need a mechanism that leads to the formation of a energetically favorable compound such as RbN_3. While the mechanism is a topic for further investigation, it is clear that chemical reactions are taking place in the cell. Our results suggest that this long-term cell whitening may be less of a concern in K-Rb hybrid or pure K SEOP cells. A picture of the two cells used during the *in situ* optical pumping tests after exposure is shown in Fig. 10 showing the white film. There could have been a different variable causing this difference in white film formation, hence further study of the difference between Rb and K-Rb or K cells is needed.

An empty GE180 cell open to atmosphere and the cell Lykurgos were also exposed to the full flux PF1B beam in prior tests without heating or optical pumping. Both cells were exposed for about 1 week and showed a formation of a brown film. However, when cell Lykurgos was later heated

FIG. 10. (Color online) The cells Orvieto, a K-Rb hybrid cell (left), and cell Lottie, a pure Rb cell (right). Despite being in the beam for over ten times as long, cell Orvieto only shows traces of a white film in an area of the cell where a blockage of hot air flow by the cell mount may have caused a cold spot on the cell. Cell Lottie, the pure Rb cell, shows a relatively uniform white film over its surface.

to optical pumping temperature (i.e., >170 °C) in the laboratory, the brown film largely disappeared and a white film eventually began to form after several cooling-heating cycles and additional tests involving neutron exposure during optical pumping, suggesting the formation of a stable chemical compound in the cell. As stated earlier, the alkali-metal vapor pressure of cell Lykurgos seemed unmodified after this prolonged exposure and the alkali-metal relaxation rates for this cell as a function of [Rb] were measured to be the same within uncertainties before and after exposure. The cell T_1 or Γ_{cell} measured in laboratory conditions for cells used in the NPDGamma experiment seems to imply a change in Γ_{cell} after the formation of white film caused by the neutron exposure cannot account for the observed long-term reductions in P_{He}.

F. Double cells

As a possible solution to many of the observed problems, two chambered cells with one chamber for optical pumping connected by a diffusion tube to another chamber for the target cell have been proposed. Such cells have been applied successfully as a solution for particle beam experiments to eliminate the alkali-metal depolarization effects [51,52]. However, for the case of charged particle beams the ^{3}He additionally experiences direct polarization relaxation from the particle bombardment that is not related to the alkali-metal polarization and must be continually refreshed using a high spin-exchange rate in the optical pumping cell to maintain a suitable ^{3}He polarization level.

For our case, the basic principle is simply to separate the degrading effects on the alkali-metal polarization and optical pumping process caused by the neutron capture by separating the NSF chamber from the optically pumped volume. A double chamber cell, called Gemini, was constructed and prepared at ISIS. It has a spherical optical pumping chamber made of GE180 glass which is connected by a 3 mm inner diameter, 10-cm-long tube to a Si-windowed Pyrex bodied spin filter chamber [53] which was designed to have the same volume as the optical pumping chamber. A picture of this cell is given in Fig. 11.

FIG. 11. (Color online) The two chambered cell named "Gemini" created for tests. The optical pumping portion is made of blown GE180 glass and the NSF portion is a Pyrex body with Si windows. The ^{3}He spin-relaxation time was 200 h with a 2 h ^{3}He polarization transfer time between the chambers.

While this cell has not yet been tested conclusively in a neutron beam, it should not suffer the alkali relaxation effects observed in this experiment. Furthermore, cell whitening issues should no longer be a concern since any chemical deposits produced in the NSF portion will be confined to that chamber by the thin transfer tube. The neutron portion of this cell was exposed to the full beam for over four hours while performing optical pumping on the other chamber. Despite a longer total exposure time than cell Lottie it did not show evidence of a white film in either chamber.

The cell T_1 and polarization transfer time can be measured directly with our NMR FID system. We normally observed the NMR FID amplitude on the cold NSF volume, but both chambers can be monitored simultaneously. The cell is polarized to an arbitrary level, then the polarization is destroyed selectively in the NSF chamber by applying an rf field generated by a three turn coil of wire driven with a function generator at the ^{3}He Larmor frequency. Then the recovery of the ^{3}He polarization is recorded over time with the NMR FID system. A discussion on the calculation of ^{3}He transfer times between double chambered cells can be found in Ref. [51].

Using these methods cell Gemini has a measured ^{3}He polarization transfer time of 2 h from one chamber to the other and a 200 h ^{3}He T_1 spin-relaxation time at room temperature. The polarization transport between the two cells should be good given the transport is fast compared to the average T_1 of the entire cell. Further, we experimentally observed the ^{3}He polarization recovers to $\simeq 50\%$ of the initial value in the NSF chamber after the selective depolarization test. Since the two chambers are of similar volume this implies good polarization transport between the chambers despite the long transfer tube. Polarization maintenance should also be good given typical spin-exchange time constants of about 10 h for a cell this size. More work is being done to characterize this cell. A similar one made entirely of GE180 with a hybrid K-Rb mixture was constructed and is being tested at NIST. Work is being done to determine the achievable polarization of ^{3}He in these cells.

Ever improved results with *in situ* polarized double chambered cells for particle beams are being reported as the techniques of hybrid SEOP [23] and narrowed-band lasers [22] are being implemented. Values of P_{He} in their double cells

FIG. 12. (Color online) The two chambered cell named "Roadrunner" created several years ago at NIST. The ^{3}He spin-relaxation time was 220 h in the laboratory and 135 h in the *in situ* apparatus installed on the thermal high-flux neutron test beam. This cell was designed for an optical pumping axis parallel to the neutron beam whereas our magnetic cavities are for perpendicular neutron and optical pumping axes. Thus, the stem on the optical pumping volume (right) is not optimal for our conditions because the optical pumping light must pass through this stem which blocks and distorts the collimated optical pumping beam.

are now reaching the 70% level in laboratory conditions [52,54], similar to the levels obtained in single NSF cells also polarized in laboratory conditions using the same techniques [26]. While the cells used as particle beam targets experience depolarization due to direct ^{3}He relaxation, they have still been able to maintain P_{He} of 50%–60% during bombardment [54]. As a further proof of principle for neutron applications we polarized a small double cell called Roadrunner *in situ* on the thermal high-flux neutron test beam at the ILL. This beamline was described briefly in Sec. II B.

Cell Roadrunner, shown in Fig. 12, was prepared several years ago at NIST but never used for neutron tests. Cell Roadrunner contains approximately 3 bar of ^{3}He at room temperature; consequently, it should have about 3.9 bar of ^{3}He in the NSF chamber when the optical pumping chamber is heated to 180 °C given the optical pumping chamber was about 45 cm^3 and the NSF chamber was about 21 cm^3. The optical pumping chamber is a 4.5 cm diameter sphere and the NSF chamber is a 1.5 cm long by 5 cm diameter cylinder connected by a 4 mm I.D. tube about 10 cm long. The room temperature T_1 of this cell is 220 h in laboratory conditions; in the *in situ* system we measured it to be 135 h.

The pressure length product of the NSF cell was measured to be 4 bar cm with the optical pumping cell at 25 °C and therefore about 5.2 bar cm with the optical pumping cell at optical pumping temperature of 180 °C. Assuming a thermal distribution of flux at 1.8 Å the neutron absorption of this cell should be around 50% for unpolarized ^{3}He and 46% at $P_{\mathrm{He}}=70\%$. Thus, the neutron capture for this cell is $(1.1-1.2\times 10^9)$ $\mathrm{cm}^{-2}\ \mathrm{s}^{-1}$ for the measured thermal flux density of 2.4×10^9 $\mathrm{cm}^{-2}\ \mathrm{s}^{-1}$ depending on P_{He}. This would lie between the full flux and 8.5% flux points on the log scale used in Fig. 9.

This cell was polarized *in situ* for a time in the absence of neutron flux while observing the ^{3}He polarization rate with a version of an NMR FID system developed at Sheffield University [55]. At time $t=8.5$ h the neutron beam was opened while continuously optically pumping the cell and observing the NMR FID. The exposure lasted for 9.5 h which was longer than $\Gamma_{\mathrm{He}}=7.2$ h for our conditions, thus any significant change in the steady-state value of P_{He} would have been apparent. As can be seen in Fig. 13, the observed Γ_{He} appears unaffected by the exposure to neutron flux. Since the strong component of gamma radiation and fast neutrons on the thermal high-flux test beamline caused significant background in the neutron detectors, TOF calibration of P_{He} was not possible on this beam. However, the P_{He} remaining in the cell after this neutron exposure test was measured some time later on a different neutron beam using methods similar to those described earlier in Sec. II A, except with a monochromatic, i.e., single wavelength, beam.

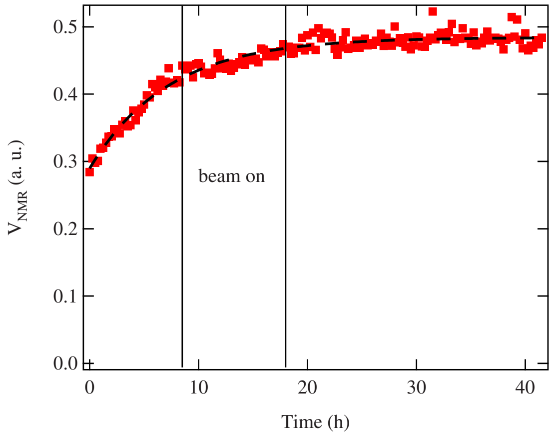

FIG. 13. (Color online) The relative $P_{\mathrm{He}}\propto V_{\mathrm{NMR}}$ via NMR FID (red squares) was fit to an exponential and shows an optical pumping time constant of 7.2 h (dotted black line). From time=8.5 h until 18 h, the cell was exposed to a thermal neutron flux density of 2.4×10^9 $\mathrm{cm}^{-2}\ \mathrm{s}^{-1}$. Unlike the single cell Orvieto shown in Fig. 4 the ^{3}He polarization and the spin-exchange rate were robust against the high neutron flux density and the cell obtained saturation $P_{\mathrm{He}}>54\%$ as determined in subsequent neutron absorption measurements on a different beamline taken after this data with the remaining polarization in the cell.

The cell was removed from the *in situ* system and transported to the laboratory in a small permanent magnet magicbox cell transporter [56]. The cell thus experienced several transports and was in nonideal magnetic conditions plus an elapsed time of about 6 h before neutron measurement. During this time we estimate that it lost 6% (relative) or more of its initial polarization. Despite the elapsed time, and the ^{3}He relaxation caused by the nonideal magnetic-field environments and transports, the initial P_{He} at the beginning of this neutron calibration was 50%. We do note this cell was designed for a solenoid geometry. Looking at Fig. 12 there is a stem on the optical pumping chamber used to prepare the cell that is in line with the NSF chamber. For our geometry the optical pumping light has to pass through and around this stem, most likely creating dark spots and thus lowering the average P_{A} in the optical pumping volume and lowering P_{He}. As can be seen from the NMR FID data P_{He} was in saturation (i.e., >99% of the maximum) at the end of the measurement when the optical pumping was stopped.

Consequently, this cell obtained relatively high saturation polarization, $>54\%$ which was unaffected by the absorbed neutron flux. The cell does not show signs of whitening in either chamber after exposure for 9.5 h. Given cell Roadrunner had a similar total neutron capture in this test to that of the single cell Lottie, discussed above in Sec. III E, this is a positive result. The next step would be to show that this system, and cell, can be stable over weeks or months and also to explore the maximum attainable P_{He} with optimization of parameters. However, these results look promising for the principle of a double chamber cell under such conditions.

IV. DISCUSSION

A. Comparison with prior alpha-particle results

The magnitude of alkali-metal relaxation was unexpected from prior experience with SEOP polarized ^{3}He targets [57]. In that work the volume of fully polarized alkali-metal atoms was estimated to be reduced to 0.6 times its normal value when a sealed SEOP cell was exposed to a particle flux of 1.1×10^{12} s^{-1} of 18 MeV alpha particles. The beam was stated to have a cross-sectional area of 0.07 cm^2 which was 10% of the cell's cross-sectional area thus the alpha-particle flux density was 1.6×10^{13} cm^{-2} s^{-1}. This implies a factor of 1.7 increase in the alkali-metal spin-relaxation rate by the following argument valid for the narrow-band dye laser used in that work. Since SEOP cells are optically very thick if the atoms are unpolarized, the light can only penetrate portions of the cell that are virtually fully polarized. The light attenuation then depends only on the alkali-metal relaxation rate Γ_{A} and the volume of the atoms that can be polarized with a given laser power $\mathcal{P}$ is simply

$$V=\frac{\mathcal{P}}{h\nu[\mathrm{Rb}]\Gamma_{\mathrm{A}}}, \tag{5}$$

where $h\nu$ is the energy of the optical pumping photons. This shows the inverse relationship between the polarized volume and the spin-relaxation rate [58]. While the alpha beam in that work was ≈3 mm in diameter, i.e., 10% of the volume of the 1 cm diameter cell, for our estimates we will consider the alpha-beam-induced effects to be spread out over the whole volume of the cell. We assume a volume averaged effect here because, as we will discuss in Sec. IV B, it seems that at least a significant fraction of the relaxation in the neutron case is likely to be caused by long-lived molecular species or clusters which can then diffuse to the cell walls.

The cell used in the alpha-particle beam had a ^{3}He pressure of 571 mbar (434 torr) and a N_2 pressure of 201 mbar (153 torr). It was held at a operating temperature of 190 °C corresponding to an assumed alkali-metal vapor density of 6×10^{14} atoms cm^{-3}. Using this information we estimate the alkali-metal relaxation rate without the alpha beam incident on the cell to be $\Gamma_{\mathrm{A}}=356$ s^{-1}, using the information summarized in Ref. [26]. With the alpha-particle beam on, we therefore estimate

$$\Gamma_{\alpha}=\left(\frac{1}{0.6}-1\right)\Gamma_{\mathrm{A}}=237\ \mathrm{s}^{-1} \tag{6}$$

to be the alpha-particle-induced relaxation rate.

The total amount of energy the α beam deposits in the cell is a property of the ion stopping power of the gas in the target cell. The stopping power of 18 MeV alpha particles in ^{3}He and N_2 is 0.476 MeV cm^2 mg^{-1} and 0.303 MeV cm^2 mg^{-1}, respectively, where the value for ^{3}He was scaled by 4/3 from the value for ^{4}He [59]. Using this, for their cell which was 3.5 cm long, we find a deposited energy of 361 keV for each alpha particle slowed in the cell. Taking 32 eV as the energy per ion for ^{3}He and 15 eV for N_2 [60], we estimate an ionization production for each alpha particle to be 3.7×10^3 $^3\mathrm{He}^+$ and 1.6×10^4 N_2^+. The total ionization rate per unit volume of cell was therefore

$$R_{\alpha}=2.0\times10^4\frac{1.6\times10^{13}\ \mathrm{cm}^{-2}\ \mathrm{s}^{-1}}{3.5\ \mathrm{cm}}=9.1\times10^{16}\ \mathrm{cm}^{-3}\ \mathrm{s}^{-1}. \tag{7}$$

For neutrons, the energy released for each neutron absorbed is 764 keV [61]. As stated before the cross section is nearly completely spin dependent and has a $1/v$ dependence, where v is the neutron velocity. The transmission of the neutron beam for an unpolarized ^{3}He cell is given by $\exp[-n\sigma(v)l]$, where n is the ^{3}He number density, $\sigma(v)$ is the absorption cross section as a function of v the neutron velocity, and l is the cell length. A typical optimized ^{3}He cell for neutron applications has an opacity $n\sigma l>1$; in practice the pressure length product is optimized so the neutron absorption of a polarized ^{3}He cell is 70%–80%. In our case, since the ^{3}He was not polarized during our γ_{A} measurements, the neutron absorption as seen in Table I was higher. Making the simplification that neutrons are fully absorbed, at the maximum ILL flux density of 4.7×10^9 cm^{-2} s^{-1}, the ionization rate per unit volume of the cell for a NSF cell of the same composition and length as the alpha-particle cell would be

$$R_n=\frac{R_{\alpha}}{0.1}\frac{4.7\times10^9}{1.6\times10^{13}}\frac{764}{361}=0.0062R_{\alpha}, \tag{8}$$

where 0.1 is the ratio of the alpha-beam area to the area of the cell in that work. The absolute ionization is just a function of deposited energy and independent of the actual alpha-particle beam size, but since our neutron beam covers the entire cross section of the cell we use it to calculate ionization per unit volume for the neutron case. At LANSCE or other lower flux facilities the ionization rate is correspondingly slower. Based on the ionization rates alone, one would expect that even at the ILL neutron-induced alkali-metal relaxation would be negligible, especially with the much higher power lasers now available that can handle much higher spin-relaxation rates.

However, the dependence of the relaxation on ionization rate or charged-particle flux is not necessarily linear. As seen from Fig. 9, the total neutron-induced relaxation rate scales roughly with the square root of the flux. Although we do not have a model for the beam-induced alkali spin relaxation we note that the square-root dependence is consistent with recombination-limited ionization, assuming that the dominant species causing spin relaxation of the alkali-metal atoms is proportional to the concentration of the dominant ionic species in the gas. In this case, the ion density would obey the rate equation

$$\frac{dn_i}{dt} = R - \beta n_i^2, \tag{9}$$

where, as before, R is the ionization rate per unit volume and β is the recombination rate coefficient. We have assumed that the electron and ion densities are equal and that the recombination mechanism is not a three-body recombination with a charged particle as the third body. Thus, in steady state the ion density is

$$n_i = \sqrt{R/\beta}. \tag{10}$$

This argument also assumes that there is a single dominant ion species or that the recombination rates of different species are approximately the same. In any case, since the ionization rate is proportional to the ionizing beam flux, the relaxation rate in this model would be proportional to the square root of the beam flux. This square-root dependence was not checked for the alpha-particle experiment. Further, for the neutron-induced alkali-metal relaxation described in Sec. III D, there appears to be a fast and a slow component possibly implying two mechanisms in the neutron case whereas we have no information on the time evolution of the alkali-metal relaxation in the alpha-particle experiment.

Assuming the square-root scaling to hold for the comparison of alpha and neutron relaxation rates, one would now estimate

$$\Gamma_n = \sqrt{\frac{R_n}{R_\alpha}}\Gamma_\alpha = 19\ \text{s}^{-1} \tag{11}$$

at full ILL flux. Again, such a small increase in the relaxation rate would be easily handled by the pumping lasers. For clarity we point out this estimate is for the electron relaxation rate which is the measured rate times the slowing-down factor. The slowing-down factor varies from 10.8 at low alkali-metal polarization to 5.44 at high-alkali-metal polarization for a pure Rb cell; therefore, this number must be divided by $\simeq 6-10$, depending on the alkali-metal polarization, to compare it to the numbers for γ_A shown in Fig. 9 which were taken at low alkali-metal polarization.

However, a highly localized effect would cause these estimates to increase such that the alpha-particle beam-induced relaxation could equal the neutron-induced alkali-metal relaxation. However, the P_A dropping to 0 coincident with the alpha-particle beam, and thus the alkali-metal relaxation becoming arbitrarily large compared to the optical pumping rate in this area, cannot be fully explained with the values given in that work. If $P_\text{A}=0$ in the alpha-particle beam, because in the geometry of that experiment where the optical pumping light was transverse to the alpha-particle beam, it would also create a shadow caused by the high alkali-metal relaxation area blocking the pump laser light from part of the cell. But by geometric arguments this would only lower the observed cell-averaged alkali-metal polarization to 80% whereas they observed 60% from measurements of P_He [57]. Thus, some spreading of the alpha-particle beam or the ionization is needed to make agreement with their measurement and support the hypothesis of a beam-localized effect. But even if the alpha-beam effect was beam localized, there would still be differences with the neutron case. The observation of the long time constant for neutrons, discussed in Sec. IV B below, seems to imply that a species that persists in the absence of the beam is responsible for a notable fraction of the relaxation in the neutron beam case. Therefore, this portion of the effect must be volume averaged and independent of beam size for the neutron case.

B. Neutron-induced alkali-metal relaxation

From Fig. 9, the relaxation rate in the neutron-induced relaxation is many times greater than the above estimate would predict. At full ILL flux the beam induced alkali-metal relaxation was $\Gamma_n=(1180\pm 30)\ \text{s}^{-1}$ for the Rb cells with nitrogen partial pressures between 0.1 and 0.12 bar, 45 times greater than expected based on the alpha-beam results. Additionally, the observed time constant of 300 s for buildup (or decay) of the additional spin-relaxation rate is quite puzzling. This time constant is incompatible with diffusion time constants for small molecules, ions, and atoms at atmospheric pressures. Thus, any normal atomic and molecular species should reach a steady-state population within at most a few seconds of the introduction of the neutron beam into the cell.

Looking again at Fig. 9 we point out the magnitude of the fast component of the increase in alkali-metal relaxation. While the true time constant of this increase is difficult to determine, subsequent tests were performed on the thermal high-flux test neutron beam which was described in Sec. III D. This fast component seems to be nearly instantaneous with the exposure to neutron flux, ≤ 1 s with accuracy limited by the opening time of the neutron shutter used. This fast component accounts for perhaps half of the total Γ_n in typical SEOP NSF cells thus any eventual mechanism or combination of mechanisms must account for the two time scales.

The most natural explanation for a 300 s time constant would be activation of an unstable nuclear species in the cell or cell walls by the neutron beam. However, this seems unlikely because the candidates for activation, such as aluminum, are not present in sufficient quantities to produce enough beta emissions to materially increase the ionization rate over that produced by the neutrons. For aluminum, which is a beta emitter with a half life of 134 s, the absorption cross section is 0.231 b. Therefore, for a typical cell made of GE180 glass which has a density of 2.76 g cm^{-3} and has an Al_2O_3 composition of 14.3% with a nominal 3 mm thickness, the neutron absorption rate would be 4.5×10^6 cm^{-2} s^{-1} for the full flux of the PF1B beam. In steady state the neutron absorption and nuclear decay, and thus beta emission rates, will be equal. Thus, there is a factor of about 1000 less beta particles emitted as compared to the neutron capture rate in the cell. In addition, the stopping power of the gas in the cell is low for beta particles, on the order of 2×10^{-3} MeV cm^2 mg^{-1} in either ^{3}He or N_2 for beta particles of 1.243 MeV, the average beta energy from an Al decay. Thus the ionization created in the cell by such sources would be over 10^5 smaller than from the neutron beam itself accounting for the 10^3 difference in particle density and 10^2 difference in deposited energy per particle. Of the other major elements in the glass, Si, Ca, Ba, and O, the nuclear half lives for Si, Ca, and Ba are much different than 300 s and the absorption cross section of the most abundant isotope of O, ^{16}O (99.8%) is small at 0.0001 b. Thus, it seems clear that the β emissions from the glass are not sufficient to cause the long time constant effect because the ionization caused by activation is orders of magnitudes smaller than that of the absorption by the ^{3}He itself.

Another possibility for the relaxation source is the formation of clusters large enough to diffuse to the walls slowly. A $\tau = 300$ s diffusion time would require a diffusion coefficient on the order of

$$D = \frac{L^2}{\pi^2 \tau} = 0.008 \ \text{cm}^2\ \text{s}^{-1}, \tag{12}$$

where L is the cell length. This is a factor of about 60 smaller than the diffusion coefficient of Rb in He [62]. The diffusion coefficient is inversely proportional to the area of the cluster and we estimate that a cluster diameter of about $d = 6$ nm would be required, with this number obtained by assuming a Rb-He cross section of 50 Å^2 and scaling by 60 to get the cross-sectional area of the cluster. Assuming that the spin-relaxation cross section is equal again to the geometric cross section of the cluster, and that the atom's full angular momentum is lost in each collision, one would require a cluster density of

$$\begin{aligned} n_C &= \frac{\Gamma_n}{v \pi (d/2)^2} \\ &= \frac{1180 \ \text{s}^{-1}}{5 \times 10^4 \ \text{cm s}^{-1} \times 3000 \ \text{Å}^2} \\ &= 7 \times 10^{10} \ \text{cm}^{-3}, \end{aligned} \tag{13}$$

where $v = 5 \times 10^4$ cm s^{-1} is the thermal velocity of Rb at SEOP temperatures.

It does seem important to note that one fundamental difference between charged particle beams and neutrons is that the neutron absorption process directly produces H and T ions. Thus, there is a built-in source of free H and T atoms and ions available in the neutron case. Clusters of RbH molecules were shown to be enhanced under very specific conditions where H_2 gas was intentionally added to an alkali-metal vapor cell and excited by a resonant laser [63]. Were the clusters causing our observed alkali-metal relaxation made from RbH molecules, a 6 nm diameter cluster would have about 2000 RbH molecules based on the 2.6 g cm^{-3} density of solid RbH, so that there would need to be about 1.4×10^{14} H per cm^3. The number of H (and T) atoms per unit volume produced by the ILL neutron beam at full flux over a 300 s time period is only $2 \times 4.7 \times 10^9$ s^{-1} cm^{-2} $\times 300$ s/5 cm$= 5.7 \times 10^{11}$ cm^{-3} for a 5-cm-long cell. Thus, there is simply not enough H produced by the neutron beam to produce sufficient RbH clusters of the size needed. One possible way to generate clusters of sufficient size to explain the observations is to hypothesize that the H (or T) atoms or ions act as nucleation sites for formation of Rb or Rb-N_x clusters. In this context it is interesting to note the increased relaxation observed in the high N_2 density cell.

Future work will attempt to explore the regime where the cell size is small or at least on the order of the range of the charged particles. The ranges of the 573 keV proton in 1 bar of ^{3}He or N_2 are 5.1 cm and 0.97 cm, respectively, and the ranges of the 191 keV triton are 1.9 cm and 0.27 cm, respectively [59]. While the cells in this experiment were in the regime where most of the particles are stopped, by varying the size of the cell or the gas pressure, we can explore the regime in which the charged particles do not come to rest within the gas. Tests on the pressure dependence of ^{3}He and N_2, temperature dependence, and the effect in pure Rb vs pure K should also be explored in future experiments.

C. Comparison of neutron-induced relaxation for hybrid and pure Rb cells

1. Theoretical evaluation

In this section we will estimate the demands on the optical pumping due to neutron-induced relaxation depending on the interpretation of the form of the transient relaxation mechanism, i.e., a total angular momentum, or an electron spin-randomization process. We will do this by comparing the expected transient decay rates and laser power demands for hybrid and pure Rb cells. In a hybrid cell, the K and Rb spin polarizations are strongly coupled by K-Rb spin-exchange collisions, so their electron spin polarizations are the same. The rate of change of the total angular momentum (per unit volume) of the system is

$$\begin{aligned} [\text{K}]\frac{d\langle F_z^{\text{K}}\rangle}{dt} + [\text{Rb}]\frac{d\langle F_z^{\text{Rb}}\rangle}{dt} &= -\gamma_{\text{K}}[\text{K}]\langle F_z^{\text{K}}\rangle - \gamma_{\text{Rb}}[\text{Rb}]\langle F_z^{\text{Rb}}\rangle \\ &\quad + [\text{Rb}]\mathcal{R}\left(\frac{1}{2} - \langle S_z\rangle\right). \end{aligned} \tag{14}$$

Here $\langle F_z^{\text{K}}\rangle$ and $\langle F_z^{\text{Rb}}\rangle$ are the average z component of the total angular momentum of the K and Rb atoms, $\langle S_z\rangle$ is the average z component of the electron spin, γ_{K} and γ_{Rb} are the angular momentum relaxation rates per atom for the two species (which are the same as the γ_{A} one would measure for a pure K or pure Rb cell in the $\mathcal{R} = 0$ limit), and $\mathcal{R}$ is again the optical pumping rate of the Rb atoms. In spin-temperature equilibrium, valid for the high densities of these experiments, the total angular momenta of the individual atoms are related to $\langle S_z\rangle$ by the slowing-down factors s_{K} and s_{Rb}: $\langle F_z^{\text{K}}\rangle = s_{\text{K}}\langle S_z\rangle$ and $\langle F_z^{\text{Rb}}\rangle = s_{\text{Rb}}\langle S_z\rangle$. A discussion of the derivation of slowing-down factors is given in [41]. For low polarizations, $s_{\text{K}} = 6$ and $s_{\text{Rb}} = 10.8$.

To aide the conceptual argument we present here where we wish to focus on the neutron-induced relaxation, we will assume that γ_{K} and γ_{Rb} in Eq. (14) and our following derivations are dominated by the neutron-induced relaxation, a reasonable estimate for the data at the 4.7×10^9 cm^{-2} s^{-1} flux density level where the neutron-induced relaxation was 10× the relaxation from other terms in γ_{A} for cell Orvieto and 6.5× larger for cell Lottie. If the additional terms for the alkali-metal spin relaxation in the absence of neutron flux were added in, one would simply obtain a linear interpolation between the relative efficiencies between hybrid K-Rb cells and pure Rb cells without incident neutron flux as in [26] and our comparison here for the high neutron flux density limit. Also, as in the cluster relaxation estimate above, we have assumed that the spin-relaxation mechanism causes loss in proportion to the total atomic angular momentum not just the electron portion.

Using the slowing-down factors in the right-hand side of Eq. (14) in the $\mathcal{R}=0$ limit, we get

$$(s_K\gamma_K\mathcal{D}+s_{Rb}\gamma_{Rb})\langle S_z\rangle = s_{KRb}\gamma_{KRb}\langle S_z\rangle, \tag{15}$$

where $\mathcal{D}=[\mathrm{K}]/[\mathrm{Rb}]$ and the hybrid slowing-down factor is $s_{KRb}=s_{Rb}+\mathcal{D}s_K$. For a pure Rb cell, the factor in parentheses would be simply $s_{Rb}\gamma_{Rb}=\Gamma_{Rb}$ and γ_{KRb} is thus defined as the total alkali-metal spin-relaxation rate for a hybrid cell. We note these are equivalent to the measured quantity γ_A for the cases of a pure Rb or hybrid KRb cell, respectively. For clarity we note again that Γ_A represents electron relaxation rates, which is what is normally relevant to calculate photon demands, whereas γ_A is total spin relaxation i.e., $d\langle F_z^A\rangle/dt$, where A is an unspecified alkali-metal or alkali-metal mixture and can be replaced by the alkali-metal species, K, Rb, or KRb in our notation. For cell Orvieto with $\mathcal{D}=2.2$, $s_{KRb}=24$. The ratio of fractional angular momentum loss for the K and Rb atoms can be determined from the experimental results by

$$\frac{\gamma_K}{\gamma_{Rb}} = \left(\frac{\gamma_{KRb}}{\gamma_{Rb}} - \frac{s_{Rb}}{s_{KRb}}\right)\frac{s_{KRb}}{s_K\mathcal{D}}. \tag{16}$$

If we assume that whatever the loss mechanism, each collision causes complete relaxation of the total atomic angular momentum, then we would expect $\gamma_K/\gamma_{Rb}=1$.

Now we need to relate the relaxation measurements to the laser power dissipation. Note that for the alkali-metal polarization, $P_A=2\langle S_z\rangle$ and the steady-state solution of Eq. (14) is

$$P_A = 2\langle S_z\rangle = \frac{\mathcal{R}}{\mathcal{R}+s_{KRb}\gamma_{KRb}}. \tag{17}$$

The photon scattering rate per unit volume for a hybrid cell is then

$$\Phi_{KRb} = [\mathrm{Rb}]_{KRb}\mathcal{R}(1-P_A) = s'_{KRb}\gamma_{KRb}[\mathrm{Rb}]_{KRb}P_A. \tag{18}$$

The prime on the slowing-down factor that appears here accounts for the fact that the slowing-down factor depends on the polarization; at high polarization, i.e., $P_A=1$, $s'_{KRb}=14.2$ for cell Orvieto. The KRb subscript on the rubidium density, $[\mathrm{Rb}]_{KRb}$, denotes the rubidium density in a hybrid cell which is lower than in a pure Rb cell following Raoult's law. For Rb, $s'_{Rb}=5.44$ and Eq. (18) becomes the relation for a pure Rb cell by replacing all of the subscript KRb terms by the Rb only equivalent and $s'_K=4$ for K. Assuming the polarizations are the same in both cells, we will compare the performance between a hybrid cell and a pure Rb cell under the practical condition of the same ^{3}He spin-exchange rates [26]. Equating the spin-exchange rates between the two cases,

$$\kappa_{Rb}[\mathrm{Rb}] = [\mathrm{Rb}]_{KRb}(\kappa_{Rb}+\mathcal{D}\kappa_K), \tag{19}$$

where [Rb] is the rubidium density in a pure Rb cell and κ_{Rb} and κ_K are the Rb-^{3}He and K-^{3}He spin-exchange rate coefficients.

Thus, using the relations in Eqs. (15) and (19) and the assumption that $\gamma_{Rb}=\gamma_K$ and substituting into Eq. (18) we find the ratio of the photon scattering in the pure Rb case, Φ_{Rb}, to the photon scattering rate in the hybrid case, Φ_{KRb}, to be

$$\frac{\Phi_{Rb}}{\Phi_{KRb}} = \frac{s'_{Rb}\gamma_{Rb}[\mathrm{Rb}]}{s'_{KRb}\gamma_{KRb}[\mathrm{Rb}]_{KRb}} = \frac{1+\mathcal{D}\kappa_K/\kappa_{Rb}}{1+\mathcal{D}s'_K/s'_{Rb}}. \tag{20}$$

Using measured values for the Rb-^{3}He and K-^{3}He spin-exchange rate coefficients from Refs. [34,64] the laser power demand ratio from Eq. (20) varies between unity at $\mathcal{D}=0$ and a numerical maximum of 1.1 at $\mathcal{D}=\infty$. Consequently, the neutron-induced power dissipation is about the same for both types of cells when the relaxation mechanism involves a total loss of spin angular momentum, electronic and nuclear.

We now repeat the above arguments assuming that the spin-relaxation process conserves the nuclear spin. Equation (14) becomes

$$[\mathrm{K}]\frac{d\langle F_z^K\rangle}{dt} + [\mathrm{Rb}]\frac{d\langle F_z^{Rb}\rangle}{dt} = -g_K[\mathrm{K}]\langle S_z\rangle - g_{Rb}[\mathrm{Rb}]\langle S_z\rangle + [\mathrm{Rb}]\mathcal{R}\left(\frac{1}{2}-\langle S_z\rangle\right), \tag{21}$$

where g_K and g_{Rb} are the potassium and rubidium spin-randomization rates. The measured transient decay rate at low polarizations then becomes

$$\gamma_{KRb} = \frac{g_K\mathcal{D}+g_{Rb}}{s_{KRb}} \tag{22}$$

and the ratio of spin-randomization rates as deduced from the low polarization transients is

$$\frac{g_K}{g_{Rb}} = \left(\frac{\gamma_{KRb}}{\gamma_{Rb}} - \frac{s_{Rb}}{s_{KRb}}\right)\frac{s_{KRb}}{s_{Rb}\mathcal{D}}. \tag{23}$$

If we assume that whatever the loss mechanism, each collision causes relaxation of only the electronic polarization, then we would expect $g_K/g_{Rb}=1$.

The photon scattering rate per unit volume for the electron randomization mechanism is

$$\Phi_{KRb} = [\mathrm{Rb}]_{KRb}\mathcal{R}(1-P_A) = (g_{Rb}+g_K\mathcal{D})[\mathrm{Rb}]_{KRb}P_A. \tag{24}$$

Again equating the spin-exchange rates for hybrid SEOP and pure Rb SEOP as in Eq. (19), the ratio of the photon scattering rates for the pure Rb and hybrid cases becomes

$$\frac{\Phi_{Rb}}{\Phi_{KRb}} = \frac{1+\mathcal{D}\kappa_K/\kappa_{Rb}}{1+\mathcal{D}g_K/g_{Rb}}. \tag{25}$$

Rewriting the photon scattering rate per unit volume in terms of the observed transient decay rate γ_{KRb} gives

$$\Phi_{\mathrm{KRb}} = s_{\mathrm{KRb}}\gamma_{\mathrm{KRb}}[\mathrm{Rb}]_{\mathrm{KRb}}P_{\mathrm{A}}. \qquad (26)$$

Comparing this with Eq. (18), we see that the deduced photon scattering rates under the assumption of an electron spin-randomization process differs from the total angular momentum loss assumption by the ratio of the low and high polarization slowing-down factors, i.e., less than a factor of 2. The laser power demand ratio from Eq. (25) varies between unity at $\mathcal{D}=0$ and a minimum of 0.81 at $\mathcal{D}=\infty$.

In summary, the key result of this section, the greatly increased demands on the optical pumping due to neutron-induced relaxation, are very nearly independent of the interpretation of the transient relaxation mechanisms. The photon demand caused by the neutron flux-induced alkali-metal relaxation is also nearly the same for hybrid and pure cells. However, for practical consideration, we note hybrid cells still retain their advantage of increased efficiency when all of the spin-relaxation terms are considered, especially when the magnitude of neutron-induced alkali-metal relaxation is not dominant (i.e., at lower flux density levels) and becomes comparable to or lower than the other spin-relaxation terms.

2. Experimental results

Here we consider the interpretation of the results for the Rb-K hybrid cell Orvieto, which, as seen in Fig. 9, has nearly the same relaxation rate as the pure Rb cells. In principle, this observation would provide a simple and direct test of whether the neutron-induced processes destroy total spin or only electronic spin. In practice our conclusions are limited because the two cells had differing, and not well known nitrogen densities, coupled with our experimental observation that the neutron-induced relaxation depends on nitrogen density. In addition, we only have data on a single hybrid cell.

For the case of total angular momentum destruction [Eqs. (15) and (16)], we find that the observed equality of the transient decay rates implies that $\gamma_{\mathrm{K}}/\gamma_{\mathrm{Rb}}=1$. If these cells were known to have the same nitrogen density, we would conclude that the data support a total angular momentum destruction mechanism. Although this conclusion is reasonable, the nitrogen densities in cell Orvieto and cell Lottie were not the same and are not precisely known. Coupled with our experimental observation that the neutron-induced relaxation depends on nitrogen density, we cannot make a definite conclusion.

For the case of electron spin randomization [Eqs. (22) and (23)], we obtain $g_{\mathrm{K}}/g_{\mathrm{Rb}}=0.55$, implying that the electron randomization rates (assuming that this is indeed the mechanism) would be smaller for K. However, if the beam effects scale linearly with nitrogen density, scaling the measured values for cell Orvieto and cell Lottie, this would make the deduced g_{K} and g_{Rb} at fixed nitrogen density nearly equal. Again a definite conclusion cannot be made.

D. Impacts for practical neutron applications

The levels of flux explored in these tests are much higher than experienced in the majority of applications which propose to use ^{3}He as a neutron polarizer or analyzer. Since the alkali-metal relaxation in our measurement at the 4×10^8 cm^{-2} s^{-1} flux level showed a manageable increase in alkali-metal relaxation and a modest 4% reduction in alkali-metal polarization, it is apparent that in applications even with a flux density of 1×10^6 cm^{-2} s^{-1} to 1×10^7 cm^{-2} s^{-1} should be largely unaffected. This class of neutron instrumentation includes nearly all situations where the ^{3}He is used as an analyzer, all monochromatic beams with the exception of some instruments using a velocity selector ($\Delta E \simeq 10\%$) and most time-of-flight instrumentation on reactor sources provided the ^{3}He is installed after part of the chopper system because there the time averaged flux is greatly reduced.

For the remaining situations such as certain instruments on the modern generation of pulsed sources and fundamental physics beamlines using the maximum intensity of neutrons available which will have fluxes of 10^8 neutron cm^{-2} s^{-1} or more, a system could readily be designed to withstand the increased alkali-metal relaxation with better optimization or more laser power if the cell degrading effects of the neutrons were eliminated. Should this prove not to be possible, we believe the two chamber cell holds the most promise for *in situ* polarization of the ^{3}He gas. Double chamber cells have been used successfully for years in nuclear and particle physics experiments [51,52] where their performance is continually increasing such that currently results of $P_{\mathrm{He}}\simeq70\%$ in cell of volumes comparable to NSF cells are being reported when not exposed to the particle beam which causes direct ^{3}He relaxation in their case [54].

Large diameter-volume double cells have been constructed at ISIS and NIST which are optimized for neutron applications. Each of these cells shows good ^{3}He polarization and T_1 relaxation times of over 200 h, with a ^{3}He polarization transfer time of 1–2 h. Further work will show the maximum obtainable polarizations for these cells which we expect to approach or exceed 70% similar to current single cells. The tests performed on cell Roadrunner in this work where $P_{\mathrm{He}}>54\%$ were obtained *in situ* during neutron exposure are a promising indicator. Finally, for situations where the beam intensity is increased with neutron focusing techniques, we believe that either single cells with higher laser power or double cells could be employed as the engineering situation is simplified by the small focused beam, and thus smaller cell size.

V. CONCLUSION

We have explored the effects caused by intense neutron absorption on *in situ* polarized ^{3}He using the SEOP method. We have identified a strong alkali-metal relaxation process that may be due to relaxation mechanisms peculiar to neutron absorption in ^{3}He. The measured relaxation, which appears to be the sum of a fast component (<1 s) and a slow component, is observed to scale as the square root of the neutron flux, consistent with the relaxation processes being associated with steady-state ion densities in the cell. Strangely, the slow component of the relaxation rate builds up and decays with a time constant that is much longer than typical atomic diffusion times. In addition, after substantial neutron exposure a white residue forms in the cell and degrades the optical properties of the cell. Further work is necessary to determine the origins of these effects. For practical applications, the information provided in this paper should provide a useful guide for near-term planning for polarized ^{3}He usage on neutron instruments.

ACKNOWLEDGMENTS

We would like to thank the ILL Millennium Program and the European Commission under the Sixth Framework Programme through the Key Action: Strengthening the European Research Area, Research Infrastructures, Contract No. RII3-CT-2003-505925 for funding this work and the *in situ* SEOP apparatus. We also greatly acknowledge Ken Andersen and the technical support of the ILL ^{3}He group, IN22 staff, and the glass shops at Heidelberg University and NIST as well as the members of the NPDGamma collaboration whose kind communication enabled us to prepare for this experiment. The contributions of T.R.G. (NIST) and W.C.C. (Indiana University) were partially supported by the U.S. Department of Energy.

---

[1] K. P. Coulter, T. E. Chupp, A. B. McDonald, C. D. Bowman, J. D. Bowman, J. J. Szymanski, V. Yuan, G. D. Cates, D. R. Benton, and E. D. Earle, Nucl. Instrum. Methods Phys. Res. A **288**, 463 (1990).

[2] M. Batz, S. Baessler, W. Heil, E. W. Otten, D. Rudersdorf, J. Schmiedeskamp, Y. Sobolev, and M. Wolf, J. Res. Natl. Inst. Stand. Technol. **110**, 293 (2005).

[3] T. R. Gentile *et al.*, Physica B **356**, 96 (2005).

[4] S. Page *et al.*, J. Res. Natl. Inst. Stand. Technol. **110**, 215 (2005).

[5] K. H. Andersen, R. Cubitt, H. Humblot, D. Jullien, A. Petoukhov, F. Tasset, C. Schanzer, V. R. Shah, and A. R. Wildes, Physica B **385-386**, 1134 (2006).

[6] J. R. Stewart *et al.*, Physica B **385-386**, 1142 (2006).

[7] U. Keiderling, A. Wiedenmann, A. Rupp, J. Klenke, and W. Heil, Meas. Sci. Technol. **19**, 034009 (2008).

[8] V. Hutanu, M. Meven, and G. Heger, Physica B **397**, 135 (2007).

[9] E. Lelièvre-Berna *et al.*, Physica B **356**, 141 (2005).

[10] W. C. Chen, G. Armstrong, Y. Chen, B. Collett, R. Erwin, T. R. Gentile, G. L. Jones, J. W. Lynn, S. McKenney, and J. E. Steinberg, Physica B **397**, 168 (2007).

[11] M. Sharma *et al.*, Phys. Rev. Lett. **101**, 083002 (2008).

[12] M. A. Bouchiat, T. R. Carver, and C. M. Varnum, Phys. Rev. Lett. **5**, 373 (1960).

[13] T. G. Walker and W. Happer, Rev. Mod. Phys. **69**, 629 (1997).

[14] F. D. Colegrove, L. D. Schearer, and G. K. Walters, Phys. Rev. **132**, 2561 (1963).

[15] P. Nacher and M. Leduc, J. Phys. (France) **46**, 2057 (1985).

[16] A. K. Petoukhov *et al.*, Physica B **385-386**, 1146 (2006).

[17] V. Hutanu, S. Masalovich, M. Meven, O. Lykhvar, and G. Heger, Neutron News **18**, 14 (2007).

[18] J. Becker, W. Heil, B. Krug, M. Leduc, M. Meyerhoff, P. Nacher, E. W. Otten, T. Prokscha, L. D. Schearer, and R. Surkau, Nucl. Instrum. Methods Phys. Res. A **346**, 45 (1994).

[19] M. Abboud, A. Sinatra, X. Maitre, G. Tastevin, and P. Nacher, Europhys. Lett. **68**, 480 (2004).

[20] A. Nikiel, T. Palasz, M. Suchanek, M. Abboud, A. Sinatra, Z. Olejniczak, T. Dohnalik, G. Tastevin, and P.-J. Nacher, Eur. Phys. J. Spec. Top. **144**, 255 (2007).

[21] B. Chann, E. Babcock, L. W. Anderson, T. G. Walker, W. C. Chen, T. B. Smith, A. K. Thompson, and T. R. Gentile, J. Appl. Phys. **94**, 6908 (2003).

[22] E. Babcock, B. Chann, I. A. Nelson, and T. G. Walker, Appl. Opt. **44**, 3098 (2005).

[23] E. Babcock, I. A. Nelson, S. Kadlecek, B. Driehuys, L. W. Anderson, F. W. Hersman, and T. G. Walker, Phys. Rev. Lett. **91**, 123003 (2003).

[24] T. R. Gentile, W. C. Chen, G. L. Jones, E. Babcock, and T. G. Walker, J. Res. Natl. Inst. Stand. Technol. **110**, 299 (2005).

[25] W. C. Chen, R. Erwin, J. W. McIver III, S. Watson, C. B. Fu, T. R. Gentile, J. A. Borchers, J. W. Lynn, and G. L. Jones, Physica B **404**, 2663 (2009).

[26] W. C. Chen, T. R. Gentile, T. G. Walker, and E. Babcock, Phys. Rev. A **75**, 013416 (2007).

[27] Y. S. Lee, G. Kim, V. R. Skoy, and T. Ino, J. Korean Phys. Soc. **48**, 233 (2006).

[28] W. T. Lee (private communication).

[29] G. L. Jones *et al.*, Physica B **385-386**, 1131 (2006).

[30] T. E. Chupp *et al.*, Nucl. Instrum. Methods Phys. Res. A **574**, 500 (2007).

[31] H. Abele *et al.*, Nucl. Instrum. Methods Phys. Res. A **562**, 407 (2006).

[32] E. Babcock, S. Boag, K. H. Andersen, M. Becker, C. Beecham, F. Bordenave, J. Chastagnier, W. C. Chen, R. Chung, T. E. Chupp, S. Elmore, P. Fouilloux, T. R. Gentile, D. Jullien, E. Lelievre-Berna, P. Mouveau, A. Petoukhov, M. Revert, and T. Soldner, Physica B **404**, 2655 (2009).

[33] S. Boag, E. Babcock, K. H. Andersen, M. Becker, T. R. Charlton, W. C. Chen, R. M. Dalgliesh, S. D. Elmore, C. D. Frost, T. R. Gentile, R. Lopez Anton, S. R. Parnell, A. K. Petoukhov, M. W. A. Skoda, and T. Soldner, Physica B **404**, 2659 (2009).

[34] B. Chann, E. Babcock, L. W. Anderson, and T. G. Walker, Phys. Rev. A **66**, 032703 (2002).

[35] E. Babcock, I. A. Nelson, S. Kadlecek, and T. G. Walker, Phys. Rev. A **71**, 013414 (2005).

[36] E. Babcock *et al.*, Physica B **397**, 172 (2007).

[37] L. W. Anderson, F. M. Pipkin, and J. C. Baird, Phys. Rev. **116**, 87 (1959).

[38] W. Franzen, Phys. Rev. **115**, 850 (1959).

[39] D. R. Rich *et al.*, Nucl. Instrum. Methods Phys. Res. A **481**, 431 (2002).

[40] G. E. Lighting Component Sales, Bldg. 315D, 1975 Noble Rd., Cleveland, OH 44117. Certain trade names and company products are mentioned in the text or identified in an illustration in order to adequately specify the experimental procedure and equipment used.

[41] M. E. Wagshul and T. E. Chupp, Phys. Rev. A **49**, 3854

(1994).

[42] S. Boag, Ph.D. thesis, University of Nottingham, 2009.

[43] National Nuclear Data Center, http://www.nndc.bnl.gov/

[44] A. V. Overberghe, Ph.D. thesis, University of Heidelberg, Heidelberg, Germany, 2006.

[45] R. E. Jacob, J. Teter, B. Saam, W. C. Chen, and T. R. Gentile, Phys. Rev. A **69**, 021401(R) (2004).

[46] E. Babcock, B. Chann, T. G. Walker, W. C. Chen, and T. R. Gentile, Phys. Rev. Lett. **96**, 083003 (2006).

[47] L. D. Schearer and G. K. Walters, Phys. Rev. **139**, A1398 (1965).

[48] A. K. Petoukhov *et al.* (unpublished).

[49] K. D. Bonin, T. G. Walker, and W. Happer, Phys. Rev. A **37**, 3270 (1988).

[50] M. V. Romalis, E. Miron, and G. D. Cates, Phys. Rev. A **56**, 4569 (1997).

[51] T. E. Chupp, R. A. Loveman, A. K. Thompson, A. M. Bernstein, and D. R. Tieger, Phys. Rev. C **45**, 915 (1992).

[52] K. Kramer, X. Zong, R. Lu, D. Dutta, H. Gao, X. Qian, Q. Ye, X. Zhu, T. Averett, and S. Fuchs, Nucl. Instrum. Methods Phys. Res. A **582**, 318 (2007).

[53] Hellma France SARL, 35 Rue de Meaux, 75019 Paris, France; certain trade names and company products are mentioned in the text or identified in an illustration in order to adequately specify the experimental procedure and equipment used.

[54] J. Singh, P. Dolph, K. Mooney, V. Nelyubin, A. Tobias, T. Averett, and G. Cates, in *Proceedings of SPIN 2008* (American Institute of Physics, New York, 2009).

[55] S. R. Parnell, E. B. Woolley, S. Boag, and C. D. Frost, Meas. Sci. Technol. **19**, 045601 (2008).

[56] A. K. Petoukhov *et al.*, Nucl. Instrum. Methods Phys. Res. B **560**, 480 (2006).

[57] K. P. Coulter, A. B. McDonald, G. D. Cates, and W. Happer, Nucl. Instrum. Methods Phys. Res. A **276**, 29 (1989).

[58] T. E. Chupp, M. E. Wagshul, K. P. Coulter, A. B. McDonald, and W. Happer, Phys. Rev. C **36**, 2244 (1987).

[59] J. P. Biersack and L. G. Haggmark, Nucl. Instrum. Methods **174**, 257 (1980); software at www.srim.org

[60] S. C. Curran, *Beta and Gamma-Ray Spectroscopy* (North-Holland, Amsterdam, 1955).

[61] G. F. Knoll, *Radiation Detection and Measurement*, 3rd ed. (Wiley, New York, 2000).

[62] M. Aymar, M. A. Bouchiat, and J. Brossel, J. Phys. (France) **30**, 619 (1969).

[63] A. Tam, G. Moe, and W. Happer, Phys. Rev. Lett. **35**, 1630 (1975).

[64] E. Babcock, Ph.D. thesis, University of Wisconsin-Madison, 2005.